

1 **Isoprene emissions in Africa inferred from OMI observations of formaldehyde columns**

2 Marais, E.A<sup>1</sup>.; D.J. Jacob<sup>1,2</sup>; T.P. Kurosu<sup>3</sup>; K. Chance<sup>4</sup>; J.G. Murphy<sup>5</sup>; C. Reeves<sup>6</sup>; G. Mills<sup>6</sup>; S.  
3 Casadio<sup>7</sup>; D.B. Millet<sup>8</sup>; M.P. Barkley<sup>9</sup>; F. Paulot<sup>2</sup>; J. Mao<sup>10</sup>

4 1. Earth and Planetary Sciences, Harvard University, Cambridge, MA, USA.

5 2. School of Engineering and Applied Sciences, Harvard University, Cambridge, MA, USA.

6 3. Earth Atmospheric Science, Jet Propulsion Laboratory, Pasadena, CA, USA.

7 4. Harvard-Smithsonian Center for Astrophysics, Cambridge, MA, USA.

8 5. Department of Chemistry, University of Toronto, Toronto, Canada.

9 6. School of Environmental Sciences, University of East Anglia, Norwich, UK.

10 7. Instrument Data quality Evaluation and Analysis (IDEAS), Serco Spa Via Sciadonna 24,  
11 00044 Frascati (Roma), Italy.

12 8. Institute on the Environment, University of Minnesota, St. Paul, MN, USA.

13 9. EOS Group, Department of Physics and Astronomy, University of Leicester, Leicester, UK.

14 10. Atmospheric and Oceanic Sciences, Princeton University, Princeton, NJ, USA.

15 Author Emails:

16 D.J. Jacob (djacob@fas.harvard.edu)

17 T.P. Kurosu (thomas.kurosu@jpl.nasa.gov)

18 K. Chance (kchance@cfa.harvard.edu)

19 J.G. Murphy (jmurphy@chem.utoronto.ca)

20 C. Reeves (c.reeves@uea.ac.uk)

21 G. Mills (G.Mills@uea.ac.uk)

22 S. Casadio (Stefano.Casadio@serco.com)

23 D.B. Millet (dbm@umn.edu)

24 M.P. Barkley (mpb14@leicester.ac.uk)

25 F. Paulot (paulot@seas.harvard.edu)

26 J. Mao (ingqium@princeton.edu)

27

28

29 **Abstract**

30 We use 2005-2009 satellite observations of formaldehyde (HCHO) columns from OMI to  
31 infer biogenic isoprene emissions at monthly  $1^{\circ}\times 1^{\circ}$  resolution over the African continent. Our  
32 work includes new approaches to remove biomass burning influences using OMI absorbing  
33 aerosol optical depth data (to account for transport of fire plumes) and anthropogenic influences  
34 using AATSR satellite data for persistent small-flame fires (gas flaring). The resulting biogenic  
35 HCHO columns ( $\Omega_{\text{HCHO}}$ ) follow closely the distribution of vegetation patterns in Africa. We  
36 infer isoprene emission ( $E_{\text{ISOP}}$ ) from the local sensitivity  $S = \Delta\Omega_{\text{HCHO}}/\Delta E_{\text{ISOP}}$  derived with the  
37 GEOS-Chem chemical transport model using two alternate isoprene oxidation mechanisms, and  
38 verify the validity of this approach using AMMA aircraft observations over West Africa and a  
39 longitudinal transect across central Africa. Displacement error (smearing) is diagnosed by  
40 anomalously high values of  $S$  and the corresponding data are removed. We find significant  
41 sensitivity of  $S$  to  $\text{NO}_x$  under low- $\text{NO}_x$  conditions that we fit to a linear function of tropospheric  
42 column  $\text{NO}_2$  from OMI. We estimate a 40% error in our inferred isoprene emissions under high-  
43  $\text{NO}_x$  conditions and 40-90% under low- $\text{NO}_x$  conditions. Comparison to the state-of-science  
44 MEGAN inventory indicates a large overestimate of central African rainforest emissions in that  
45 inventory.

46

47

## 48 **1. Introduction**

49 Isoprene ( $\text{CH}_2=\text{C}(\text{CH}_3)\text{CH}=\text{CH}_2$ ) is the dominant non-methane volatile organic compound  
50 (NMVOC) emitted by vegetation, accounting for about 50% of global NMVOC emissions  
51 according to current inventories (Guenther et al., 2006). It is a major precursor of organic aerosol  
52 (Claeys et al., 2004; Henze and Seinfeld, 2006; Kroll et al., 2006) and of tropospheric ozone  
53 (Fiore et al., 2011; Tao et al., 2003; Trainer et al., 1987), thus impacting air quality, climate, and  
54 human health. Isoprene also affects the abundance of OH, the main atmospheric oxidant  
55 (Lelieveld et al., 2008; Ren et al., 2008). Satellite observations of formaldehyde (HCHO), a high-  
56 yield product of isoprene oxidation, can provide useful constraints on isoprene emissions  
57 (Palmer et al., 2003). Here we use HCHO satellite observations from the Ozone Monitoring  
58 Instrument (OMI) to better quantify isoprene emissions from the African continent. Africa  
59 appears as a major isoprene source region in global HCHO satellite data (Meyer-Arnek et al.,  
60 2005; de Smedt et al., 2008), yet it has thus far received little attention.

61 Isoprene emission inventories in atmospheric chemistry models generally follow the  
62 Guenther et al. (1995) framework, which uses base emissions for different ecosystem types  
63 modulated by local environmental factors. These inventories are constructed by extrapolation of  
64 limited ecosystem data and best understanding of processes, and are commonly called “bottom-  
65 up”. Arneth et al. (2008) point out that there is considerable uncertainty in bottom-up isoprene  
66 emission inventories, more than is apparent from the spread of values in the literature, as all tend  
67 to rely on the same limited data and algorithm framework. Direct isoprene emission  
68 measurements in Africa are particularly limited, consisting of a few data for tropical rainforests  
69 (Greenberg et al., 1999; Klinger et al., 1998; Serça et al., 2001), woodlands (Greenberg et al.,

70 2003, 1999; Otter et al., 2002), savannas (Guenther et al., 1996; Harley et al., 2003; Klinger et  
71 al., 1998; Otter et al., 2002; Saxton et al., 2007), and shrublands (Otter et al., 2002).

72 An alternate “top-down” approach for estimating isoprene emissions is to use HCHO  
73 column measurements made by satellites from solar backscatter in the 330-360 nm absorption  
74 bands (Chance et al., 2000). Isoprene has an atmospheric lifetime of typically less than 1 h  
75 against oxidation by OH, producing HCHO which has a lifetime of 1-2 h against photolysis and  
76 oxidation by OH. This adds to the HCHO background originating mainly from the oxidation of  
77 methane. Thus the HCHO columns measured from space can be related to the underlying  
78 isoprene emission (Palmer et al., 2003). Contributions from other biogenic or anthropogenic  
79 NMVOCs are generally much weaker because emissions are lower and/or HCHO production is  
80 slower (Palmer et al., 2003). Inference of isoprene emissions from HCHO column measurements  
81 by the GOME (1995 launch), SCIAMACHY (2002 launch), and OMI (2004 launch) satellite  
82 instruments has been reported in a number of studies for North America (Abbot et al., 2003;  
83 Millet et al., 2008; Palmer et al., 2006, 2003), Asia (Fu et al., 2007), Europe (Curci et al., 2010;  
84 Dufour et al., 2009), South America (Barkley et al., 2008), and globally (Shim et al., 2005;  
85 Stavrakou et al., 2009a). Biomass burning makes a major seasonal contribution to HCHO in the  
86 tropics, and was screened by Barkley et al. (2008) using satellite fire count and NO<sub>2</sub> data.

87 Relating HCHO columns to isoprene emission requires a quantitative relationship between  
88 the two obtained with a chemical transport model (CTM). Most of our current understanding of  
89 isoprene chemistry has been developed for high concentrations of nitrogen oxide radicals (NO<sub>x</sub> ≡  
90 NO+NO<sub>2</sub>) that originate in the atmosphere from combustion sources and soil emissions. Under  
91 these high-NO<sub>x</sub> conditions (>1 ppb NO<sub>x</sub>) the organic peroxy radicals (RO<sub>2</sub>) produced from  
92 isoprene oxidation react preferentially with NO. The resulting HCHO yield is relatively well

93 quantified and is mostly realized in the first stage of isoprene oxidation (Millet et al., 2006;  
94 Palmer et al., 2003). Under low-NO<sub>x</sub> conditions more typical of Africa, the RO<sub>2</sub> radicals may  
95 instead react with HO<sub>2</sub> or isomerize (Peeters et al., 2009), modifying and delaying HCHO yields  
96 (Mao et al., 2010; Palmer et al., 2006, 2003). Delay in HCHO production causes smearing in the  
97 local relationship between isoprene emission and the HCHO column (Palmer et al., 2003). This  
98 smearing can in principle be resolved in a formal inversion accounting for CTM transport (Shim  
99 et al., 2005; Stavrou et al., 2009a), but this requires more confidence than is probably  
100 warranted in the coupling between chemical and transport timescales.

101 Here we use a 5-year record of OMI HCHO data (2005-2009) to constrain isoprene  
102 emissions from the African continent. We convert HCHO columns to isoprene emissions by  
103 using the GEOS-Chem CTM with updated isoprene chemistry (Paulot et al., 2009a, 2009b). We  
104 introduce a new method to screen biomass burning influence based on OMI observations of  
105 aerosol absorption optical depth (AAOD) (Torres et al., 2007) and also screen urban and gas  
106 flaring influences. We use aircraft observations from the African Monsoon Multidisciplinary  
107 Analysis (AMMA) campaign in West Africa during July-August 2006 (Murphy et al., 2010;  
108 Reeves et al., 2010; Stone et al., 2010) to test the GEOS-Chem simulation of isoprene chemistry  
109 and estimate the smearing in the isoprene-HCHO relationship. We also derive a new approach to  
110 account for the NO<sub>x</sub> dependence of the isoprene-HCHO relationship using OMI NO<sub>2</sub> data.

111

## 112 **2. Constructing a data set of OMI biogenic HCHO columns**

### 113 **2.1 Slant columns**

114 The Ozone Monitoring Instrument (OMI) (Levelt et al., 2006) was launched onboard the  
115 Aura satellite in 2004. It has spatial resolution of 13×24 km<sup>2</sup> at nadir, an equator crossing time of

116 13h38, and achieves daily global coverage with a cross-track swath width of 2600 km. HCHO  
117 slant columns ( $\Omega_s$ ) are a standard product from the OMI instrument, obtained by spectral fitting  
118 of backscattered solar radiation in the 327.5 – 356.5 nm window ([http://www.cfa.harvard.edu/  
119 atmosphere/Instruments/OMI/PGEReleases/READMEs/OMHCHO\\_README.pdf](http://www.cfa.harvard.edu/atmosphere/Instruments/OMI/PGEReleases/READMEs/OMHCHO_README.pdf)). We use  
120 OMHCHO Version 2.0 (Collection 3) retrievals for 2005-2009 from the NASA Data and  
121 Information Services Center ([http://disc.sci.gsfc.nasa.gov/Aura/dataholdings/OMI/omhcho\\_  
122 v003.shtml](http://disc.sci.gsfc.nasa.gov/Aura/dataholdings/OMI/omhcho_v003.shtml)). We exclude observations that (1) do not pass all fitting and statistical quality checks  
123 specified in the standard product (i.e. *MainDataQualityFlag* = 0), (2) have a cloud fraction > 0.4  
124 determined from the OMI O<sub>2</sub>-O<sub>2</sub> cloud product (Stammes et al., 2008), or (3) are affected by the  
125 OMI row anomaly ([http://www.knmi.nl/omi/research/  
product/rowanomaly-background.php](http://www.knmi.nl/omi/research/product/rowanomaly-background.php)).

126 The OMI data feature a slow increase in the baseline  $\Omega_s$  with time over 2005-2009 that  
127 likely reflects degradation of the instrument. We correct for this using observations over the  
128 remote Pacific (40-50°S, 150-160°W) where the OMI data are essentially noise. Following the  
129 methodology of Kim et al. (2011) we fit a 4<sup>th</sup> order polynomial function to the baseline slant  
130 column  $\Omega_{s,b}$  over that region as a function of time  $t$ :

131

$$132 \quad \Omega_{s,b} = -2.0 \times 10^3 t^4 + 9.6 \times 10^6 t^3 - 1.3 \times 10^{10} t^2 + 7.5 \times 10^{12} t + 2.5 \times 10^{15} \quad (1)$$

133

134 where  $\Omega_{s,b}$  is in molecules cm<sup>-2</sup> and  $t$  is in days ( $t = 1$  on 1 January 2005). We remove  $\Omega_{s,b}$   
135 calculated with (1) from the OMI measurement of  $\Omega_s$  and will refer to the residual as  $\Omega_s$  in what  
136 follows.

137 We thus compile 8-day average values for  $\Omega_s$  on a  $1^\circ \times 1^\circ$  (lat $\times$ lon) grid for 2005-2009  
138 (Fig. 1a). The slant column fitting uncertainty for a single observation is  $8 \times 10^{15}$  molecules  $\text{cm}^{-2}$   
139 on average. 8-day and  $1^\circ \times 1^\circ$  averaging reduces the uncertainty to  $1-2 \times 10^{15}$  molecules  $\text{cm}^{-2}$ .

140

## 141 **2.2 Removing biomass burning and anthropogenic influences**

142 We remove biomass burning and anthropogenic influences from the  $\Omega_s$  data in order to  
143 isolate the biogenic component. The standard procedure for removing biomass burning is to use  
144 space-based observations of fire counts (Barkley et al., 2008; Jaeglé et al., 2005). We begin with  
145 this approach by using MODIS day and night fire counts from the Terra satellite. The data are  
146 provided daily at a resolution of  $1 \times 1 \text{ km}^2$  (Giglio et al., 2003) and we average them for 8 days on  
147 the same  $1^\circ \times 1^\circ$  grid as  $\Omega_s$ . We exclude persistent fires associated with large industrial and urban  
148 areas of Cairo (Egypt), the Mpumalanga Highveld region (South Africa), and the Niger Delta  
149 (Nigeria). We then remove as contaminated by biomass burning all gridsquares with non-zero  
150 fire counts for the concurrent and preceding 8-day periods.

151 Screening only on the basis of fire counts is insufficient as it does not account for the  
152 long-range transport of HCHO in biomass burning plumes. Plume influences on HCHO far  
153 downwind of fires in Africa are evident from Lagrangian analyses of satellite data (Meyer-Arnek  
154 et al., 2005) and AMMA aircraft data (Janicot et al., 2008; Mari et al., 2008; Murphy et al., 2010;  
155 Reeves et al., 2010). Solar backscatter satellite instruments retrieve both HCHO and  $\text{NO}_2$ , and  
156 Barkley et al. (2008) previously used  $\text{NO}_2$  as an additional filter to screen against biomass  
157 burning in tropical South America. We find that this filter is inadequate for Africa because the  
158 atmospheric lifetime of  $\text{NO}_x$  emitted from biomass burning is only a few hours whereas the

159 influence of fires on HCHO is more sustained owing to continued oxidation of precursor  
160 NMVOCs (Alvarado et al., 2010; Hobbs et al., 1996; Trentmann et al., 2003).

161 Our method to diagnose biomass burning plumes is to use the AAOD product from OMI  
162 for the same scenes as HCHO (Torres et al., 2007). Absorbing aerosol is conserved in the plume  
163 in the absence of precipitation. We use the level 2 version 3 gridded OMI AAOD product  
164 ([http://disc.sci.gsfc.nasa.gov/Aura/data-holdings/OMI/omaeruv\\_g\\_v003.shtml](http://disc.sci.gsfc.nasa.gov/Aura/data-holdings/OMI/omaeruv_g_v003.shtml)), provided at  
165  $0.25^\circ \times 0.25^\circ$  horizontal resolution, and average it over 8-day periods on the same  $1^\circ \times 1^\circ$  grid as  
166  $\Omega_s$ . The product includes separate contributions from dust and smoke aerosol but separation  
167 between the two can be difficult (Ahn et al., 2008) and we find that smoke AAOD is elevated in  
168 dusty regions. To address this problem, we subdivide the continent latitudinally into the  
169 Mediterranean strip (north of  $20^\circ\text{N}$ ), northern Africa ( $4^\circ\text{N}$ - $19^\circ\text{N}$ ), equatorial Africa ( $5^\circ\text{S}$ - $4^\circ\text{N}$ ),  
170 and southern Africa (south of  $5^\circ\text{S}$ ). For each region we plot the 5-year frequency distribution of  
171 OMI smoke AAOD, as shown in Fig. 2 for southern Africa. This separates biomass burning and  
172 non-biomass burning scenes into two populations, and we remove the biomass burning scenes.  
173 The smoke AAOD thresholds are 0.02, 0.07, 0.05, and 0.04 for the Mediterranean strip, northern  
174 Africa, equatorial Africa, and southern Africa, respectively.

175 Large dust influence is also problematic in the interpretation of HCHO slant columns  
176 because of scattering and absorption by the dust. Northern and equatorial Africa can be very  
177 dusty. We filter out high dust scenes with the OMI dust AAOD product previously described  
178 using a threshold value of 0.1, above which the radiative interference would be of concern.

179 The OMI HCHO data show high values over Nigeria (Fig. 1a) that may reflect urban  
180 NMVOC emissions in Lagos (Hopkins et al., 2009; Oketola and Osibanjo, 2007; Reeves et al.,  
181 2010), biofuel use that is particularly dense in rural Nigeria (Yevich and Logan, 2003), and gas

182 flaring in the Niger Delta (Casadio et al., 2011). Other African countries that practice gas flaring  
183 related to the oil and gas industry include Libya, Algeria, Angola, Egypt, Gabon, Sudan, Congo  
184 and Tunisia (Casadio et al., 2011). We remove HCHO associated with gas flaring by using gas  
185 flare hotspots retrieved in the 1.6  $\mu\text{m}$  band (Algorithm3 or ALGO3) from the Advanced Along  
186 Track Scanning Radiometer (AATSR) satellite instrument (Casadio et al., 2011). We average the  
187 AATSR fire counts over the same  $1^\circ \times 1^\circ$  grid and 8-day averaging period as OMI and remove  
188 gridsquares with non-zero gas flares. Over Nigeria the enhancements in HCHO occur beyond the  
189 region of flaring, which may reflect pollution transport as well as Lagos emissions and intense  
190 biofuel use. We therefore remove a more extensive  $3^\circ \times 3^\circ$  area around the gridsquares affected by  
191 flaring in Nigeria. The AATSR data do not extend over South Africa due to noise from the South  
192 Atlantic Anomaly (Casadio et al., 2011), but we find that the six oil refineries in South Africa  
193 [SAPIA, 2008] are not associated with elevated HCHO in the OMI data of Fig. 1a. We therefore  
194 see no need for additional screening.

195 Our filtering scheme to remove biomass burning, dust, and anthropogenic contributions  
196 from the OMI  $\Omega_s$  observations is summarized in Fig. 3. It removes 40% of observations over  
197 Africa on average and 70-80% in the southern hemisphere during the dry season. Figure 1 shows  
198 the mean OMI  $\Omega_s$  observations for 2005-2009 before (a) and after (b) application of the filtering  
199 scheme. The filtered observations are taken to represent biogenic HCHO in what follows.

200

### 201 **2.3 Conversion to vertical columns**

202 The slant column  $\Omega_s$  obtained by spectral fitting is related to the true vertical column  
203  $\Omega_{\text{HCHO}}$  by an air mass factor ( $\text{AMF} = \Omega_s / \Omega_{\text{HCHO}}$ ) obtained with a radiative transfer model. We use  
204 the formulation of Palmer et al. (2001), which calculates the AMF as the vertical integral of the

205 relative vertical distribution of HCHO (shape factor) weighted by altitude-dependent coefficients  
206 (scattering weights). The scattering weights are functions of viewing geometry, surface albedo,  
207 and atmospheric scattering by air molecules, aerosols, and clouds. Cloud fraction and cloud top  
208 pressure are from the OMI O<sub>2</sub>-O<sub>2</sub> cloud product (Stammes et al., 2008). The LIDORT radiative  
209 transfer model (Spurr et al., 2001) is used to calculate scattering weights for individual scenes.  
210 Clouds are represented by Lambertian surfaces with an albedo of 0.8, as recommended by  
211 Koelemeijer and Stammes (1999), and consistent with the O<sub>2</sub>-O<sub>2</sub> cloud algorithm. Surface albedo  
212 for the African continent is from the OMI reflectance climatology at 345 nm (Kleipool et al.,  
213 2008). HCHO and aerosol vertical distributions are monthly mean values from the GEOS-Chem  
214 CTM, described in Sect. 3.

215 We find that 62% of the spatial variability in the annual average AMFs over Africa is  
216 driven by OMI surface albedo. The AMF is close to unity for much of the continent (average  
217 1.2), with larger values over the Sahara and Namib Deserts (high albedo) and lower values over  
218 central Africa (low albedo). Figure 1c shows the resulting annual mean distribution of HCHO  
219 vertical columns  $\Omega_{\text{HCHO}}$ . We see that most of the variability in  $\Omega_{\text{HCHO}}$  is present in the slant  
220 column data and thus is not driven by the AMF. The  $\Omega_{\text{HCHO}}$  patterns match closely the  
221 distribution of major land types in Africa (Fig. 1d), supporting the interpretation of HCHO as a  
222 proxy for isoprene emission. Maximum values are found over evergreen broadleaf forests in the  
223 tropics. Low values occur over barren, shrub, herbaceous, and cultivated vegetation. Small-scale  
224 biogenic features are apparent such as the forested belt along the east coast of South Africa,  
225 crops along the Nile River, and the coastal vegetated Mediterranean strip.

226

227

## 228 3. GEOS-Chem model

### 229 3.1 General description

230 We use the GEOS-Chem global 3D CTM (version 8-03-01, <http://geos-chem.org>) to (1)  
231 estimate the vertical distribution of HCHO for use in the AMF calculation and (2) quantify the  
232 relationship between isoprene emissions and HCHO column abundance. GEOS-Chem is driven  
233 by Goddard Earth Observing System (GEOS-5) assimilated meteorological data from the NASA  
234 Global Modeling and Assimilation Office (GMAO). The GEOS-5 meteorological data have a  
235 native horizontal resolution of  $0.5^\circ \times 0.67^\circ$  with 72 vertical pressure levels and 6-h temporal  
236 frequency (3-h for surface variables and mixing depths). We use data for year 2006 and degrade  
237 the horizontal resolution to  $2^\circ \times 2.5^\circ$  for input to GEOS-Chem. The model results presented here  
238 are from one year of simulation (2006) following one year of spinup for chemical initialization.

239 Biogenic emission of isoprene is calculated locally in GEOS-Chem using the MEGAN  
240 v2.1 inventory (Guenther et al., 2006), with modifications described below. Anthropogenic  
241 emissions of  $\text{NO}_x$  in Africa are from the EDGAR v2.0 inventory (Olivier et al., 1996). Biomass  
242 burning NMVOC and  $\text{NO}_x$  emissions are from the Global Fire Emissions Database v2 (Van der  
243 Werf et al., 2006).  $\text{NO}_x$  emissions from soils and fertilizer use are from the algorithm of Yienger  
244 and Levy (1995) as implemented by Wang et al. (1998).

245 Dry deposition in GEOS-Chem follows the standard resistance-in-series scheme of  
246 Wesely (1989). In that scheme, gases are deposited as determined by their Henry's law solubility  
247 and their surface reactivity (referenced to ozone). Here we have updated the dry deposition of  
248 HCHO and other oxygenated products of isoprene oxidation including methyl vinyl ketone  
249 (MVK), methacrolein (MACR), glycolaldehyde, and dicarbonyls to have the same surface  
250 reactivity as ozone, based on observational evidence of rapid deposition (Karl et al., 2009, 2004;

251 Misztal et al., 2010; Pugh et al., 2010; Sumner et al., 2001) and following the recommendation of  
252 Karl et al. (2010). We also include in the model wet and dry deposition of isoprene peroxides  
253 and epoxydiols using respective Henry's law constants of  $1.7 \times 10^6 \text{ M atm}^{-1}$  (US EPA, 2011) and  
254  $1.3 \times 10^8 \text{ M atm}^{-1}$  (Eddingsaas et al., 2010).

255 We account in this GEOS-Chem version for the grid-scale transport of isoprene peroxides  
256 produced from oxidation of isoprene under low- $\text{NO}_x$  conditions. Previous versions of GEOS-  
257 Chem did not include this transport, leading to an underestimate in the spatial displacement  
258 (smearing) between isoprene emission and the resulting HCHO columns.

259

### 260 **3.2 Improved treatment of isoprene chemistry**

261 GEOS-Chem includes detailed ozone- $\text{NO}_x$ -VOC-aerosol coupled chemistry originally  
262 described by Bey et al. (2001) and Park et al. (2004), with recent updates described by Mao et al.  
263 (2010). We have updated the rate coefficients for the reactions of  $\text{HO}_2$  with  $> \text{C}_2$  peroxy radicals  
264 to Eq. (iv) of Saunders et al. (2003). At 298 K the rate coefficient doubles from 0.8 to  $1.6 \times 10^{-11}$   
265  $\text{cm}^3 \text{ molecule}^{-1} \text{ s}^{-1}$  relative to previous versions of GEOS-Chem, increasing the relative  
266 importance of the low- $\text{NO}_x$  isoprene oxidation pathway.

267 The standard isoprene oxidation scheme used in GEOS-Chem is largely based on  
268 Horowitz et al. (1998). As with all conventional schemes, it leads to OH titration by isoprene  
269 under low- $\text{NO}_x$  conditions, but this titration is not seen in observations (Lelieveld et al., 2008;  
270 Ren et al., 2008). We implement as alternate isoprene oxidation scheme in GEOS-Chem the  
271 Paulot et al. (2009b) mechanism, where regeneration of OH under low- $\text{NO}_x$  conditions takes  
272 place via oxidation of epoxydiol species produced from oxidation of isoprene hydroperoxides.  
273 Isomerization of the isoprene peroxy radicals leading to the formation of hydroperoxyaldehydes,

274 described in Peeters et al. (2009) and Peeters and Müller (2010), is not included in our  
275 mechanism as experimental evidence indicates that it is too slow to compete with reaction with  
276 HO<sub>2</sub> (Crouse et al., 2011). We compare below results from the “standard” and “Paulot”  
277 schemes to assess the degree of uncertainty in simulating HCHO yields. The “standard”  
278 chemistry scheme is that in version 8-03-01 of GEOS-Chem with updated RO<sub>2</sub> + HO<sub>2</sub> kinetics as  
279 described above.

280 Figure 4 shows the time-dependent yields of HCHO from isoprene oxidation calculated in  
281 the DSMACC box model (Emmerson and Evans, 2009) for the standard and Paulot schemes as  
282 implemented in GEOS-Chem with different NO<sub>x</sub> levels. Each simulation uses fixed  
283 concentrations of O<sub>3</sub> (28 ppbv), CO (150 ppbv), and NO<sub>x</sub> (0.01, 0.1, and 1 ppbv). Isoprene is  
284 initially 1 ppbv and allowed to decay. The temperature is 298 K. Diurnally varying photolysis  
285 frequencies are calculated for clear sky at the Equator with surface albedo of 0.1 and an ozone  
286 column of 260 Dobson units. Under high-NO<sub>x</sub> conditions (1 ppbv), we find that the ultimate  
287 HCHO yield is approached within a few hours and is similar for both schemes. Under low-NO<sub>x</sub>  
288 conditions (0.1 ppbv), the ultimate yield is 10-20% lower and takes 1-2 days to achieve, again  
289 with similar values for both schemes. The largest difference is under very low NO<sub>x</sub> conditions  
290 (0.01 ppbv) where the ultimate yield is 30-40% lower than under high-NO<sub>x</sub> conditions and the  
291 timescale for reaching that yield is 5-6 days. The Paulot scheme does not show a shorter  
292 timescale for reaching the ultimate yield than the standard scheme, despite higher OH, because it  
293 generates more HCHO from later-generation isoprene oxidation products. The implications of  
294 these results for the isoprene-HCHO relationship will be discussed further in Sect. 4 in the  
295 context of GEOS-Chem results and using OMI NO<sub>2</sub> columns to identify NO<sub>x</sub> regimes.

296

### 297 **3.3 MEGAN Bottom-Up Isoprene Emission Inventory**

298 We use the MEGAN algorithm of Guenther et al. (2006) as our best prior emission  
299 estimate for isoprene to which the constraints from the OMI HCHO data can be compared. This  
300 inventory is widely used in global CTMs. Isoprene accounts for 80% of biogenic NMVOC  
301 emissions on a per-carbon basis in Africa according to MEGAN. The canopy-scale isoprene  
302 emission flux,  $E_{\text{ISOP}}$ , per unit area of Earth surface (atoms C cm<sup>-2</sup> s<sup>-1</sup>) is computed as:

$$304 \quad E_{\text{ISOP}} = E_0 \gamma_T \gamma_{\text{AGE}} \gamma_{\text{SM}} \gamma_{\text{CE}} \quad (2).$$

305  
306 Here  $E_0$  is the emission at baseline conditions of air temperature (303 K), leaf age (80% mature,  
307 10% growing, and 10% old), soil moisture (0.3 m<sup>3</sup> water m<sup>-3</sup> soil), light (1500 μmol photons m<sup>-2</sup>  
308 s<sup>-1</sup>), and leaf area index (LAI = 5). The unitless environmental scaling factors ( $\gamma$ ) describe the  
309 effects of temperature ( $T$ ), leaf age ( $\text{AGE}$ ), soil moisture ( $\text{SM}$ ), and canopy radiative environment  
310 ( $\text{CE}$ ) on  $E_0$ .  $\gamma_{\text{CE}}$  includes the effects of both LAI and light. Values of  $E_0$  are specified for five  
311 plant functional types (PFTs): broadleaf trees, needleleaf trees, grasses, crops, and shrubs. The  
312 global distribution of PFTs is taken from the biome database of Olson et al. (2001), and the  
313 distribution of trees in Africa south of the Equator is overwritten by the regional database of  
314 Otter et al. (2003). In GEOS-Chem  $E_0$  is input at 1°×1° and regridded to 2°×2.5° resolution prior  
315 to estimating  $E_{\text{ISOP}}$ .

316 Our GEOS-Chem simulation uses the environmental scaling factors  $\gamma$  as given by  
317 Guenther et al. (2006) and applied to the local GEOS-5 surface data, except for soil moisture.  
318 Stavrou et al. (2009b) found in their analysis of GOME and SCIAMACHY HCHO satellite  
319 data that water stress is an important contributor to variability of isoprene emissions over

320 southern Africa and is not well represented in MEGAN. We use here the soil moisture  
321 parameterization developed by Müller et al. (2008) and found by Ferreira et al. (2010) to achieve  
322 a good simulation of isoprene emission over West Africa during AMMA:

323

$$324 \quad \gamma_{\text{SM}} = \sum_{i=1}^n \left[ f_i \times \max \left( 0, \min \left( 1, \frac{(\theta_i - \theta_{i,w})}{0.06} \right) \right) \right] \quad (3),$$

325

326 where the summation is over  $n$  vertical soil layers,  $f_i$  is the root fraction within soil layer  $i$  such  
327 that  $\sum_{i=1}^n f_i = 1$ ,  $\theta_i$  is the degree of saturation or volumetric ratio of soil moisture to the porosity  
328 of the soil ( $\text{m}^3$  water  $\text{m}^{-3}$  air), and  $\theta_{i,w}$  is the degree of saturation at the wilting point. The GEOS-  
329 5 meteorological data provide  $\theta_i$  for two layers ( $n = 2$ ): a top soil layer (2 cm) and a root zone  
330 layer (1 m). Müller et al. (2008) used a fixed wilting point value of 0.171, but here we use  
331 gridded monthly average wilting points, ranging from 0.05 to 0.6 in Africa, from the GEOS-5  
332 catchment land surface model (Koster et al., 2000). We determine  $f_i$  within each layer using the  
333 parameterization of Zeng (2001) for dominant IGBP landcover types at  $1^\circ \times 1^\circ$  from the MODIS  
334 landcover data set (Friedl et al., 2002).

335 Our resulting global emission of isoprene in GEOS-Chem for 2006 is  $470 \text{ Tg C a}^{-1}$ , within  
336 the  $440\text{-}660 \text{ Tg C a}^{-1}$  range given by Guenther et al. (2006). Africa accounts for 20% of global  
337 isoprene emissions. Implementation of the soil moisture scaling factor  $\gamma_{\text{SM}}$  as described above  
338 reduces annual isoprene emissions by about 10% globally and 15% over Africa. The global  
339 reduction in isoprene emissions is less than the 30% reduction obtained by Müller et al. (2008),  
340 likely due to the spatially variable wilting points used here.

#### 341 4. HCHO-isoprene relationship

342 Previous interpretation of the HCHO column  $\Omega_{\text{HCHO}}$  in terms of isoprene emission using  
343 GEOS-Chem has relied on a local linear regression between the two quantities in the model  
344 (Palmer et al., 2003):

$$345 \Omega_{\text{HCHO}} = SE_{\text{ISOP}} + B \quad (4)$$

346 where  $S$  is the slope of the reduced-major-axis regression line and  $B$  is the intercept representing  
347 the background HCHO column. The value of  $S$  is determined by the HCHO yield from isoprene  
348 oxidation and by the HCHO lifetime. Millet et al. (2008) presented estimates of  $S$  for North  
349 America in summer by performing either a single regression for the ensemble of GEOS-Chem  
350 gridsquares covering North America or local regressions for individual  $2^\circ \times 2.5^\circ$  gridsquares. The  
351 first method yielded  $S = 2.4 \times 10^3$  s with high correlation ( $R^2 = 0.82$ ), while the second yielded  
352 variable slopes with an interquartile range of  $2.0\text{-}3.0 \times 10^3$  s. These values were consistent with  
353 observation-based estimates for the PROPHET forest site in Michigan ( $2.1 \times 10^3$  s) and INTEX-  
354 A aircraft observations over the eastern US ( $2.3 \times 10^3$  s) (Millet et al., 2006; Palmer et al., 2003).  
355 Over tropical South America where  $\text{NO}_x$  levels are much lower, Barkley et al. (2008) found a  
356 strong spatial correlation ( $R^2 > 0.7$ ) between  $E_{\text{ISOP}}$  and  $\Omega_{\text{HCHO}}$  in GEOS-Chem but with large  
357 seasonal variability in  $S$  – ranging from  $1 \times 10^3$  s in January-March to  $2 \times 10^3$  s in May-July.

360 Here we use our updated version of GEOS-Chem, together with observational constraints  
361 from AMMA and OMI, to examine the local  $E_{\text{ISOP}}\text{-}\Omega_{\text{HCHO}}$  relationships over Africa and their  
362 suitability for inferring isoprene emissions from the HCHO column data. We quantify the  
363 smearing of the relationship caused by delay in HCHO production from isoprene, develop a

364 parameterization for the dependence of the  $E_{\text{ISOP}}-\Omega_{\text{HCHO}}$  relationship on  $\text{NO}_x$ , and estimate the  
365 errors in the resulting isoprene emission estimates.

366

#### 367 **4.1 Smearing**

368 We first examine the extent of smearing in the HCHO-isoprene relationship over Africa  
369 using aircraft measurements of isoprene, the sum of MVK and MACR (MVK+MACR), and  
370 HCHO concentrations obtained during AMMA in West Africa in July-August 2006 (Murphy et  
371 al., 2010; Reeves et al., 2010). The AMMA wet season aircraft campaign (Redelsperger et al.,  
372 2006), based in Niamey, Niger, made latitudinal transects across sharp vegetation gradients from  
373 ocean to dense woodland to desert (Fig. 5). 19 flights were made from 20 July to 17 August,  
374 2006, mainly during daytime hours. Boundary layer winds were prevailingly from the south  
375 (West African monsoon) (Janicot et al., 2008). We exclude biomass burning plumes as  
376 diagnosed by  $> 250$  pptv acetonitrile (Commane et al., 2010; Murphy et al., 2010) as well as the  
377 flights of August 8 (Lagos urban plume) and August 15 (mesoscale convective system).

378 Figure 5 shows the AMMA flight tracks superimposed on a map of MODIS LAI for July-  
379 August 2006 (Yang et al., 2006), together with latitudinal profiles of observed and simulated  
380 isoprene, MVK+MACR, and HCHO concentrations below 900 hPa. The model is sampled along  
381 the flight tracks and at the flight times. Also included in Fig. 5 is the HCHO concentration below  
382 900 hPa inferred from OMI observations for July-August 2005-2009 averaged over the AMMA  
383 longitudinal domain ( $1-4^\circ\text{E}$ ) into  $1^\circ$  latitude bins (multi-year temporal averaging is needed to  
384 reduce measurement noise). The HCHO concentration below 900 hPa is inferred from OMI  
385 HCHO columns by using the mean HCHO vertical profile measured during AMMA (340 pptv

386 above 750 hPa and linear increase from 750 hPa to the surface). The break in the OMI data at 5-  
387 7°N reflects systematic exclusion of anthropogenic influence from Nigeria (Sect. 2.2).

388         The sharp vegetation gradients sampled in AMMA along the direction of the prevailing  
389 southerly monsoon winds make the data of great value for understanding smearing in the HCHO-  
390 isoprene relationship. We see from Fig. 5 that observed isoprene and MVK+MACR tightly  
391 follow the vegetation gradients, and this is well captured by the model. Model values are much  
392 higher than observed at 11-13°N and 7-8°N, reflecting a local overestimate of  $E_{\text{ISOP}}$  in MEGAN  
393 (Ferreira et al., 2010; Murphy et al., 2010). MVK and MACR are first-stage C<sub>4</sub> isoprene  
394 oxidation products with HCHO produced from the additional carbon atom (Paulson et al., 1992).  
395 The tightness of the isoprene-(MVK+MACR) relationship in Fig. 5, both in the observations and  
396 the model, demonstrates that there is no significant smearing and provides an important test of  
397 the isoprene oxidation scheme. Model isoprene concentrations are lower in the Paulot scheme  
398 because of OH regeneration from the RO<sub>2</sub> + HO<sub>2</sub> reaction pathway, as described in Sect. 3.2, but  
399 this has negligible impact on the simulation of (MVK+MACR).

400         The right panel of Fig. 5 shows that observed and simulated HCHO are also strongly  
401 correlated with the vegetation gradients. The AMMA observations for HCHO are much lower  
402 than the model or inferred from OMI, and we do not have an explanation for this beyond the  
403 possibility of large bias in the Hantzsch-fluorometric instrument used on the aircraft (Grossmann  
404 et al., 2003; Hak et al., 2005; Klemp et al., 2003; Still et al., 2006). Because HCHO is produced  
405 together with MVK+MACR it would be difficult to account for a model bias in HCHO but not in  
406 MVK+MACR. Tests with the model indicate little sensitivity to the assumed deposition  
407 velocities. In any case, comparison of the HCHO and isoprene latitudinal gradients shows no  
408 significant northward smearing either in the observations or the model. The strongest correlation

409 between observed isoprene and HCHO ( $R^2 = 0.86$ ) occurs for an offset of  $0.5^\circ$  north of the peak  
410 in observed isoprene ( $8\text{-}12^\circ\text{N}$ ). Smearing of  $\sim 0.5^\circ$ , combined with a mean observed southerly  
411 wind speed of  $17 \text{ km h}^{-1}$  south of  $12^\circ\text{N}$ , implies a timescale of less than a day for production of  
412 HCHO from isoprene.

413 The negligible smearing in the AMMA observations may reflect the relatively high  $\text{NO}_x$   
414 conditions. Boundary layer (i.e. below 900 hPa)  $\text{NO}_x$  concentrations in the region of isoprene  
415 emission ( $7\text{-}13^\circ\text{N}$ ) averaged 360 pptv in the observations and 310 pptv in the model, due to a  
416 mix of influences from soil, anthropogenic, and distant biomass burning sources (Hopkins et al.,  
417 2009; Reeves et al., 2010; Stewart et al., 2008). We find in GEOS-Chem that such a  $\text{NO}_x$   
418 concentration places the AMMA conditions at the threshold between the high- $\text{NO}_x$  regime  
419 (where isoprene  $\text{RO}_2$  reacts mainly with NO) and the low- $\text{NO}_x$  regime (where isoprene  $\text{RO}_2$   
420 reacts mainly with  $\text{HO}_2$ ). Stone et al. (2010) found a 70% mean contribution of the high- $\text{NO}_x$   
421 pathway during AMMA using the DSMACC box model.

422 The OMI  $\text{NO}_2$  data offer a broader perspective on  $\text{NO}_x$  regimes across Africa. Figure 6  
423 shows annual average tropospheric columns of  $\text{NO}_2$  ( $\Omega_{\text{NO}_2}$ ) from OMI (Boersma et al., 2007)  
424 for 2005-2009 and compares to the GEOS-Chem simulation for 2006. Biomass burning  
425 influence has been removed in the observations using MODIS fire counts and OMI AAOD (Sect.  
426 2.2) and in GEOS-Chem with black carbon AOD from the model, for consistency with the  
427 removal of biomass burning influence in the OMI HCHO column product. We find from the  
428 AMMA observations (Stewart et al., 2008) that, similar to HCHO,  $\text{NO}_2$  increases linearly from  
429 750 hPa to the surface. Mean  $\text{NO}_2$  observations above 750 hPa are below the limit of detection of  
430 the aircraft instrument. Thus 1 ppbv of boundary layer  $\text{NO}_x$  corresponds roughly to a  
431 tropospheric  $\text{NO}_2$  column of  $2.2 \times 10^{15}$  molecules  $\text{cm}^{-2}$ . The fitting precision of  $7\text{-}8 \times 10^{14}$

432 molecules  $\text{cm}^{-2}$  for individual OMI  $\text{NO}_2$  pixels (Boersma et al., 2007) is reduced to  $3\text{-}4 \times 10^{13}$   
433 molecules  $\text{cm}^{-2}$  for monthly mean data at  $1^\circ \times 1^\circ$  resolution, so that levels as low as  $\sim 0.02$  ppb  
434  $\text{NO}_x$  are detectable. We see in Fig. 6 that much of Africa is in an intermediate  $\text{NO}_x$  regime (0.1-  
435 1 ppb). Even in the absence of continental biomass burning influences, significant boundary  
436 layer  $\text{NO}_x$  levels are maintained in Africa by soil emissions (Jaeglé et al., 2005) and by  
437 decomposition of peroxyacetyl nitrate (PAN) originating from outside the continent (Moore and  
438 Remedios, 2010; Singh and Hanst, 1981).

439 We further examined the effect of high isoprene emissions on smearing as a result of OH  
440 titration. For this we consider the equatorial forest of central Africa ( $3^\circ\text{S}$ - $3^\circ\text{N}$ ) in July where  $\text{NO}_x$   
441 levels are moderate (average tropospheric  $\text{NO}_2$  columns of  $8.4$  and  $5.7 \times 10^{14}$  molecules  $\text{cm}^{-2}$  for  
442 OMI and GEOS-Chem, respectively), and ventilation is by a steady easterly wind. Figure 7  
443 shows the longitudinal gradients of MEGAN  $E_{\text{ISOP}}$ , OMI  $\Omega_{\text{HCHO}}$ , and model column HCHO  
444 (standard and Paulot schemes) across the region. Immediately downwind (to the west) of the  
445 rainforest is a shadow region where elevated HCHO does not correspond to collocated isoprene  
446 emission but instead reflects transport from the forest. Assuming that MEGAN correctly  
447 represents the location of isoprene emission (mainly determined by the location of the equatorial  
448 rainforest), enhancements in OMI  $\Omega_{\text{HCHO}}$  are sustained  $\sim 2\text{-}3^\circ$  west of that location. The smearing  
449 is well reproduced by the model using either the standard or Paulot scheme and the extent of  
450 smearing is not reduced in the Paulot scheme as a result of OH regeneration. Combined with a  
451 mean easterly wind speed of  $5 \text{ km h}^{-1}$  for the region, it implies a timescale of  $\sim 2\text{-}3$  days for  
452 production of HCHO from isoprene. We will see below how we can screen such shadow regions  
453 from the dataset.

454

## 455           4.2 NO<sub>x</sub> dependence

456           We now examine the variability of the  $\Omega_{\text{HCHO}}-E_{\text{ISOP}}$  relationship over Africa in GEOS-  
457 Chem measured by the local slope  $S$  in Eq. (4). This variability reflects differences in the  
458 chemical environment as well as the effect of smearing in an inhomogeneous isoprene emission  
459 field. Millet et al. (2008) previously examined the spatial variability of  $S$  over North America by  
460 constructing local  $\Omega_{\text{HCHO}}-E_{\text{ISOP}}$  regressions at the  $2^\circ \times 2.5^\circ$  grid resolution of GEOS-Chem,  
461 relying on the temperature-driven day-to-day variation of  $E_{\text{ISOP}}$  in a given gridsquare to define a  
462 dynamic range for the regression. We find that this is not an effective approach in Africa as day-  
463 to-day variability in isoprene emission is often small. We derive instead the  $\Omega_{\text{HCHO}}-E_{\text{ISOP}}$   
464 relationship in GEOS-Chem by conducting a sensitivity simulation with isoprene emissions  
465 reduced by a factor of 2 from the MEGAN values. We then infer  $S = \Delta\Omega_{\text{HCHO}}/\Delta E_{\text{ISOP}}$  for  
466 individual gridsquares and months (gridsquare-months) where  $\Delta$  is the monthly mean change  
467 relative to the standard simulation, excluding periods of biomass burning influence (diagnosed  
468 with black carbon AOD in the model). Values of  $S$  over the southeast US ( $75-100^\circ\text{W}$ ,  $27-40^\circ\text{N}$ )  
469 for June-August 2006 using this approach are  $1.9$  and  $2.0 \times 10^3$  s for the standard and Paulot  
470 schemes, respectively, similar to values reported by Millet et al. (2008, 2006) and Palmer et al.  
471 (2006).

472           Gridsquare-months affected by smearing can be diagnosed in this analysis by  
473 anomalously high values of  $S$ . We find that 41% of gridsquare-months in GEOS-Chem over  
474 Africa have  $S > 4 \times 10^3$  s, which is higher than the HCHO yields from isoprene emission would  
475 allow and reflects the effect of smearing mainly in regions where isoprene emissions are close to  
476 zero (such as the vast desert expanses as well as coastal gridsquares). Although this may seem  
477 like a large population to exclude, the corresponding area accounts for only 2% of isoprene

478 emission over Africa in MEGAN and thus is largely irrelevant for our purpose. We remove all  
479 gridsquare-months in GEOS-Chem with  $S > 4 \times 10^3$  s in what follows.

480 For the remainder of the data we find a significant dependence of  $S$  on the local  $\text{NO}_x$   
481 concentration, as would be expected from our box model results in Fig. 4. We choose to define  
482 this relationship in the model in terms of  $S$  vs.  $\Omega_{\text{NO}_2}$  so that the OMI  $\Omega_{\text{NO}_2}$  data can be applied to  
483 remove the effects of model errors in  $\text{NO}_x$ . Figure 8 shows the  $S$  values calculated for individual  
484  $2^\circ \times 2.5^\circ$  gridsquare-months over the African continent in 2006 as a function of local model  $\Omega_{\text{NO}_2}$ .  
485 The data are averaged into  $1 \times 10^{14}$  molecules  $\text{NO}_2 \text{ cm}^{-2}$  bins. For  $\Omega_{\text{NO}_2} \leq 1 \times 10^{15}$  molecules  $\text{cm}^{-2}$   
486 (equivalent to 0.6 ppbv surface  $\text{NO}_x$  using our conversion factor) we find a linear relationship  
487 between  $S$  and  $\Omega_{\text{NO}_2}$  ( $R^2 > 0.9$ ) reflecting the increasing importance of the  $\text{RO}_2 + \text{NO}$  pathway  
488 with increasing  $\text{NO}_x$ . For  $\Omega_{\text{NO}_2} > 1 \times 10^{15}$  molecules  $\text{cm}^{-2}$  we find that  $S$  levels off as the  $\text{RO}_2 +$   
489  $\text{NO}$  pathway becomes dominant. 10-20% higher HCHO yields in the Paulot scheme compared  
490 with the standard scheme are consistent with the box model results of Fig. 4. The average  $\Omega_{\text{NO}_2}$   
491 from OMI during AMMA (July-August 2006) is included in Fig. 8 for reference; we see that the  
492 AMMA conditions are at the threshold between high- $\text{NO}_x$  and low- $\text{NO}_x$  conditions, consistent  
493 with Stone et al. (2010) and our earlier discussion.

494

### 495 **4.3 Error analysis**

496 Inference of isoprene emission from OMI column HCHO involves a number of steps, all  
497 of which are prone to error. Here we estimate these different error terms and their contributions  
498 to the overall error.

499 The spectral fitting uncertainty for  $\Omega$ , observations averaged over  $1^\circ \times 1^\circ$  gridsquares and  
500 8-day periods is  $1-2 \times 10^{15}$  molecules  $\text{cm}^{-2}$  (Sect. 2.1). We find (not shown) that the model can

501 reproduce the shape of the mean HCHO vertical profile observed in AMMA (linear decrease  
502 from the surface to 750 hPa, low values above 750 hPa), suggesting that there is no particular  
503 problem in simulating the HCHO vertical shape factor under African conditions. In the absence  
504 of better information, we adopt the AMF error estimate of Millet et al. (2006) derived from  
505 aircraft observations in North America: 15% for clear sky increasing to 24% for 50% cloud  
506 cover (Millet et al., 2006). Taking a fitting error of  $2 \times 10^{15}$  molecules  $\text{cm}^{-2}$  and an AMF error of  
507 20% (since we exclude scenes with >40% cloud cover), and applying these errors in quadrature  
508 to a vertical HCHO column of  $1 \times 10^{16}$  molecules  $\text{cm}^{-2}$  with AMF of 1.2, we estimate an overall  
509 error on the OMI HCHO retrieval of  $2 \times 10^{15}$  molecules  $\text{cm}^{-2}$  or 20%.

510 Conversion of HCHO columns to isoprene emission using Eq. (4) involves errors in the  
511 slope  $S$  due both to the chemical mechanism and to smearing. Figure 8 shows that the standard  
512 and Paulot mechanisms differ by only 15% in their calculations of  $S$ , which is similar to the error  
513 estimates from Palmer et al. (2006) and Millet et al. (2008) in comparing  $S$  values from GEOS-  
514 Chem to aircraft and surface observations over the US. The error is certainly larger under low-  
515  $\text{NO}_x$  conditions where better understanding of isoprene chemistry is needed. Still, it appears that  
516 the error bars on  $S$  shown in Fig. 8 (which we attribute mainly to smearing) are larger than the  
517 errors induced by the chemical mechanism. From these error bars we derive an uncertainty in  $S$   
518 from smearing of 750 s for the low- $\text{NO}_x$  regime ( $\Omega_{\text{NO}_2} = 0.2\text{-}1 \times 10^{15}$  molecules  $\text{cm}^{-2}$ ) and 690 s  
519 for the high- $\text{NO}_x$  regime ( $\Omega_{\text{NO}_2} > 1 \times 10^{15}$  molecules  $\text{cm}^{-2}$ ).

520 Error in the OMI tropospheric  $\text{NO}_2$  column (standard deviation ( $\sigma_{\text{NO}_2}$ ) also propagates  
521 to error in the linear regression equation  $S = (1600 \pm 160) \Omega_{\text{NO}_2} + (721 \pm 114)$  for the low- $\text{NO}_x$   
522 regime (Paulot scheme in Figure 8). We use the expression from Boersma et al. [2008] to  
523 estimate  $\sigma_{\text{NO}_2}$  for 8-day average  $\Omega_{\text{NO}_2}$  observations:

524 
$$\sigma_{\text{NO}_2} = \frac{1.0 \times 10^{15} + 0.3 \times \Omega_{\text{NO}_2}}{\sqrt{8} \times \sqrt{3.5}} \quad (5),$$

525 and propagate this with the linear regression errors in the slope  $m$  ( $\sigma_m = 160$ ) and intercept  $c$  ( $\sigma_c =$   
526 114). The resulting error standard deviation  $\sigma_S$  in  $S$  is determined as

527 
$$\sigma_S = \sqrt{(m \times \sigma_{\text{NO}_2})^2 + (\Omega_{\text{NO}_2} \times \sigma_m)^2 + \sigma_c^2}$$
 and is in the range 340-440 s for  $\Omega_{\text{NO}_2}$  of 0.2-1.0  $\times$

528  $10^{15}$  molecules  $\text{cm}^{-2}$ ; smaller than the estimated smearing error of 750 s. The error in  $S$  at low  
529  $\text{NO}_x$ , adding in quadrature the contributions from smearing and from the linear regression of  $S$   
530 against  $\Omega_{\text{NO}_2}$ , is 823-870 s (35-84%).

531 The overall error in inferring isoprene emission from OMI HCHO columns, adding in  
532 quadrature the errors on the OMI retrieval of HCHO columns and the conversion of HCHO  
533 columns to isoprene emission, is 40% in the high- $\text{NO}_x$  regime and 40-90% in the low- $\text{NO}_x$   
534 regime. These errors apply to 8-day average  $1^\circ \times 1^\circ$  OMI HCHO data and could be reduced by  
535 further temporal averaging to the extent that they are random, which is difficult to assess given  
536 the uncertainties associated with the isoprene oxidation mechanism at low levels of  $\text{NO}_x$ .

537

## 538 **5. Implications for OMI-derived isoprene emissions in Africa**

539 We have presented here a new methodology for inferring isoprene emissions from HCHO  
540 satellite data and applied it to the African continent using OMI. Detailed discussion of the  
541 implications for African isoprene emissions and their dependence on environmental variables is  
542 left to a separate paper. We present here some preliminary results. For this purpose we use the  
543 2005-2009 monthly mean OMI HCHO vertical columns at  $1^\circ \times 1^\circ$  horizontal resolution derived in  
544 Sect. 2, monthly mean  $S$  values computed from GEOS-Chem with the Paulot scheme, and 2005-  
545 2009 monthly mean  $\text{NO}_2$  tropospheric column observations from OMI (Boersma et al., 2007).

546 Figure 9 shows the resulting spatial distribution of annual isoprene emissions at 12-15  
547 local time (LT) and compares to the corresponding values from the MEGAN inventory. Values  
548 are means for all  $1^\circ \times 1^\circ$  gridsquare-months that are not excluded from our analysis because of  
549 biomass burning, anthropogenic, dust, or smearing influences. Fully excluded areas are shown in  
550 grey. The right panel of Fig. 9 shows the difference between the OMI-derived emissions and  
551 values from MEGAN.

552 From the data in Fig. 9 we find that the annual mean isoprene emissions in Africa  
553 inferred from OMI ( $60 \text{ Tg C a}^{-1}$ ) are on average 22% lower than the MEGAN values ( $77 \text{ Tg C a}^{-1}$ ).  
554 Larger regional discrepancies are apparent. For example, OMI is on average 33% lower than  
555 MEGAN over the central African rainforest, while 38% higher over the southern deciduous  
556 broadleaf forests.

557

## 558 **6. Conclusions**

559 We presented a new method for inferring biogenic isoprene emissions from satellite  
560 observations of HCHO columns under the particularly challenging conditions of the tropics, and  
561 applied this method to 2005-2009 OMI HCHO observations over the African continent.

562 Removing biomass burning influence is critical for isolating the biogenic component of  
563 HCHO in the tropics. Previous procedures using satellite fire counts or  $\text{NO}_2$  columns are  
564 insufficient because they do not account for long-range transport of fire plumes. Here we used  
565 OMI observations of absorbing aerosol optical depth (AAOD) as an additional screening tool.  
566 We also identified a significant anthropogenic component over Africa associated with gas  
567 flaring, particularly in Nigeria, and removed it using small-flame satellite fire data. Our resulting

568 biogenic HCHO product shows close correspondence with the distribution of vegetation in  
569 Africa.

570         Inferring isoprene emission from HCHO column data requires knowledge of the time-  
571 dependent HCHO yield from isoprene oxidation. This is a challenge in the tropics because of the  
572 prevailing low-NO<sub>x</sub> conditions under which the isoprene oxidation mechanism is not well  
573 understood and HCHO production may be delayed. Here we used two alternate mechanisms to  
574 quantify HCHO-isoprene relationships in GEOS-Chem. The two mechanisms show a similar  
575 positive NO<sub>x</sub> dependence of the HCHO yield under low-NO<sub>x</sub> conditions, and a delay between  
576 isoprene emission and HCHO production ranging from less than a day under high-NO<sub>x</sub>  
577 conditions to several days under low-NO<sub>x</sub> conditions. This delay smears the local relationship  
578 between isoprene emission ( $E_{\text{ISOP}}$ ) and HCHO columns ( $\Omega_{\text{HCHO}}$ ).

579         We evaluated the GEOS-Chem simulation of the HCHO-isoprene relationship using  
580 aircraft observations from the AMMA campaign along a latitudinal transect of vegetation types  
581 in West Africa. Both observations and model show strong spatial correlation between isoprene,  
582 MVK+MACR (first-stage products of isoprene oxidation associated with HCHO formation), and  
583 HCHO. This implies insignificant (< 100 km) smearing in the HCHO-isoprene relationship.  
584 Inspection of longitudinal gradients across the equatorial forest of central Africa, where NO<sub>x</sub> is  
585 low, indicates smearing of ~200-300 km. This means that large isoprene source regions under  
586 low-NO<sub>x</sub> conditions produce a shadow effect downwind that affects interpretation of the local  
587 HCHO-isoprene relationship.

588         We computed local relationships between HCHO columns and isoprene emission at the  
589 2°×2.5° GEOS-Chem grid resolution and on a monthly basis by conducting a sensitivity  
590 simulation with uniformly perturbed isoprene emission and inferring the relationship  $S =$

591  $\Delta\Omega_{\text{HCHO}}/\Delta E_{\text{ISOP}}$ . Smearing was diagnosed by anomalously high  $S$  values and the corresponding  
592 scenes were excluded from further analysis. We found that  $S$  is sensitive to  $\text{NO}_x$  at levels below  
593 600 pptv (tropospheric  $\text{NO}_2$  column  $\leq 1 \times 10^{15}$  molecules  $\text{cm}^{-2}$ ). From there we used the OMI  
594  $\text{NO}_2$  column observations to diagnose  $S$  for the corresponding OMI HCHO data. The error in  
595 OMI-derived isoprene emissions is 40% at high  $\text{NO}_x$  and 40-90% at low  $\text{NO}_x$  for 8-day  $1^\circ \times 1^\circ$   
596 OMI HCHO gridsquares. Smearing makes the largest contribution to the error for both  $\text{NO}_x$   
597 regimes.

598         We presented a preliminary comparison of the OMI-derived annual mean isoprene  
599 emissions over Africa to the values computed from the bottom-up MEGAN inventory used in  
600 GEOS-Chem. The total OMI-derived isoprene emission for the African continent is 23% lower  
601 than MEGAN. Large regional discrepancies are apparent for the high-emitting evergreen  
602 broadleaf trees of central Africa and the adjacent deciduous broadleaf trees. In a follow-up paper  
603 we will exploit the OMI HCHO data to develop improved understanding of the environmental,  
604 seasonal, and interannual variations in isoprene emission over Africa using the OMI HCHO  
605 observations.

606         The two main uncertainties in using space-based HCHO column data to infer isoprene  
607 emission are (1) the isoprene oxidation mechanism as it relates to HCHO production under low-  
608  $\text{NO}_x$  conditions, (2) the coupling between transport and chemistry determining the displacement  
609 between observed HCHO columns and precursor isoprene emissions. The latter could be  
610 addressed by using a CTM adjoint inversion (Stavrakou et al., 2009a). This will eventually be  
611 necessary if we are to exploit the fine resolution of the satellite observations ( $13 \times 24 \text{ km}^2$  in nadir  
612 for OMI) to obtain correspondingly fine constraints on isoprene emission. However, the value of  
613 such an approach is hampered at present by inadequate knowledge of the time-dependent HCHO

614 yields from isoprene oxidation under low-NO<sub>x</sub> conditions, and by the difficulty of representing  
615 the coupling between transport and chemistry over timescales relevant to boundary layer mixing  
616 and mesoscale motions. Future progress most critically requires an improved understanding of  
617 isoprene oxidation chemistry through laboratory and field measurements.

618

619

620           **Acknowledgements.** This work was funded by NASA through the Aura Science Team  
621 and by a South African National Research Scholarship for Study Abroad to EAM. EAM would  
622 like to thank Omar Torres and Folkert Boersma for assistance with OMI satellite products and  
623 Sarith Mahanama and Randal Koster for providing updated soil moisture assimilated data over  
624 Africa. DBM acknowledges support from NASA ACMAP (#NNX10AG65G).

625

626 **7. References**

- 627 Abbot, D. S., Palmer, P. I., Martin, R. V., Chance, K., Jacob, D. J. and Guenther, A.: Seasonal  
628 and interannual variability of North American isoprene emissions as determined by  
629 formaldehyde column measurements from space, *Geophys. Res. Lett.*, 30,  
630 doi:10.1029/2003GL017336, 2003.
- 631 Ahn, C., Torres, O. and Bhartia, P. K.: Comparison of Ozone Monitoring Instrument UV Aerosol  
632 Products with Aqua/Moderate Resolution Imaging Spectroradiometer and Multiangle Imaging  
633 Spectroradiometer observations in 2006, *J. Geophys. Res.*, 113, doi:10.1029/2007JD008832,  
634 2008.
- 635 Alvarado, M. J., Logan, J. A., Mao, J., Apel, E., Riemer, D., Blake, D., Cohen, R. C., Min, K.-E.,  
636 Perring, a. E., Browne, E. C., Wooldridge, P. J., Diskin, G. S., Sachse, G. W., Fuelberg, H.,  
637 Sessions, W. R., Harrigan, D. L., Huey, G., Liao, J., Case-Hanks, A., Jimenez, J. L., Cubison, M.  
638 J., Vay, S. a., Weinheimer, a. J., Knapp, D. J., Montzka, D. D., Flocke, F. M., Pollack, I. B.,  
639 Wennberg, P. O., Kurten, A., Crouse, J. D., Clair, J. M. S., Wisthaler, A., Mikoviny, T.,  
640 Yantosca, R., Carouge, C. and Le Sager, P.: Nitrogen oxides and PAN in plumes from boreal  
641 fires during ARCTAS-B and their impact on ozone: an integrated analysis of aircraft and satellite  
642 observations, *Atmos. Chem. Phys.*, 10, 9739-9760, 2010.
- 643 Arneth, A., Monson, R. K., Schurgers, G., Niinemets, Ü. and Palmer, P. I.: Why are estimates of  
644 global terrestrial isoprene emissions so similar (and why is this not so for monoterpenes)?,  
645 *Atmos. Chem. Phys.*, 8, 4605-4620, 2008.
- 646 Barkley, M. P., Palmer, P. I., Kuhn, U., Kesselmeier, J., Chance, K., Kurosu, T. P., Martin, R.  
647 V., Helmig, D. and Guenther, A.: Net ecosystem fluxes of isoprene over tropical South America  
648 inferred from Global Ozone Monitoring Experiment (GOME) observations of HCHO columns,  
649 *J. Geophys. Res.*, 113, doi:10.1029/2008JD009863, 2008.
- 650 Bartholomé, E. and Belward, A. S.: GLC2000: a new approach to global land cover mapping  
651 from Earth observation data, *Int. J. of Remote Sens.*, 26, 1959-1977, 2005.
- 652 Bey, I., Jacob, D. J., Yantosca, R., Logan, J. A., Field, B. D., Fiore, A., Li, Q., Liu, H. Y.,  
653 Mickley, L. J. and Schultz, M. G.: Global modeling of tropospheric chemistry with assimilated  
654 meteorology: Model description and evaluation, *J. Geophys. Res.*, 106, 23073-23095,  
655 doi:10.1029/2001JD000807, 2001.
- 656 Boersma, K., Eskes, H., Veefkind, J. P., Brinksma, E., van der A, R., Sneep, M., van den Oord,  
657 G. H. J., Levelt, P. F., Stammes, P., Gleason, J. and Bucsela, E. J.: Near-real time retrieval of  
658 tropospheric NO<sub>2</sub> from OMI, *Atmos. Chem. Phys.*, 7, 2103–2118, 2007.
- 659 Boersma, K., Jacob, D. J., Eskes, H., Pinder, R. W., Wang, J. and van der A, R. J.:  
660 Intercomparison of SCIAMACHY and OMI tropospheric NO<sub>2</sub> columns: Observing the diurnal

661 evolution of chemistry and emissions from space, *J. Geophys. Res.*, 113,  
662 doi:10.1029/2007JD008816, 2008.

663 Casadio, S., Arino, O. and Serpe, D.: Gas flaring monitoring from space using the ATSR  
664 instrument series, *Remote Sens. Environ.*, 116, 239-249, doi:10.1016/j.rse.2010.11.022, 2011.

665 Chance, K., Palmer, P. I., Spurr, R. J. D., Martin, R. V., Kurosu, T. P. and Jacob, D. J.: Satellite  
666 observations of formaldehyde over North America from GOME, *Geophys. Res. Lett.*, 27, 3461-  
667 3464, doi:10.1029/2000GL011857, 2000.

668 Claeys, M., Graham, B., Vas, G., Wang, W., Vermeylen, R., Pashynska, V., Cafmeyer, J.,  
669 Guyon, P., Andreae, M. O., Artaxo, P. and Maenhaut, W.: Formation of secondary organic  
670 aerosols through photooxidation of isoprene, *Science*, 303, 1173-1176, 2004.

671 Commane, R., Floquet, C. F. A., Ingham, T., Stone, D., Evans, M. J. and Heard, D. E.:  
672 Observations of OH and HO<sub>2</sub> radicals over West Africa, *Atmos. Chem. Phys.*, 10, 8783-8801,  
673 2010.

674 Crounse, J. D., Paulot, F., Kjaergaard, H. G. and Wennberg, P. O.: Peroxy radical isomerization  
675 in the oxidation of isoprene, *Phys. Chem. Chem. Phys.*, 13, 13607-13613, 2011.

676 Curci, G., Palmer, P. I., Kurosu, T. P., Chance, K. and Visconti, G.: Estimating European volatile  
677 organic compound emissions using satellite observations of formaldehyde from the Ozone  
678 Monitoring Instrument, *Atmos. Chem. Phys.*, 10, 11501-11517, 2010.

679 Dufour, G., Wittrock, F., Camredon, M., Beekmann, M., Richter, A., Aumont, B. and Burrows,  
680 J. P.: SCIAMACHY formaldehyde observations: constraint for isoprene emission estimates over  
681 Europe?, *Atmos. Chem. Phys.*, 9, 1647-1664, 2009.

682 Eddingsaas, N. C., VanderVelde, D. G. and Wennberg, P. O.: Kinetics and products of the acid-  
683 catalyzed ring-opening of atmospherically relevant butyl epoxy alcohols, *J. Phys. Chem. A*, 114,  
684 8106-8113, 2010.

685 Emmerson, K. and Evans, M. J.: Comparison of tropospheric gas-phase chemistry schemes for  
686 use within global models, *Atmos. Chem. Phys.*, 9, 1831-1845, 2009.

687 Ferreira, J., Reeves, C. E., Murphy, J. G., Garcia-Carreras, L., Parker, D. J. and Oram, D. E.:  
688 Isoprene emissions modelling for West Africa: MEGAN model evaluation and sensitivity  
689 analysis, *Atmos. Chem. Phys.*, 10, 8453-8467, 2010.

690 Fiore, A., Levy II, H. and Jaffe, D. a.: North American isoprene influence on intercontinental  
691 ozone pollution, *Atmos. Chem. Phys.*, 11, 1697-1710, 2011.

692 Friedl, M., McIver, D., Hodges, J., Zhang, X., Muchoney, D., Strahler, A., Woodcock, C., Gopal,  
693 S., Schneider, A., Cooper, A., Baccini, A., Gao, F. and Schaaf, C.: Global land cover mapping  
694 from MODIS: algorithms and early results, *Remote Sens. Environ.*, 83, 287-302, 2002.

695 Fu, T.-M., Jacob, D. J., Palmer, P. I., Chance, K., Wang, Y. X., Barletta, B., Blake, D. R.,  
696 Stanton, J. and Pilling, M.: Space-based formaldehyde measurements as constraints on volatile  
697 organic compound emissions in east and south Asia and implications for ozone, *J. Geophys.*  
698 *Res.*, 112, doi:10.1029/2006JD007853, 2007.

699 Giglio, L., Descloitres, J., Justice, C. O. and Kaufman, Y. J.: An enhanced contextual fire  
700 detection algorithm for MODIS, *Remote Sens. Environ.*, 87, 273-282, 2003.

701 Greenberg, J., Guenther, A., Harley, P., Otter, L. B., Veenendaal, E. M., Hewitt, C. N., James, A.  
702 E. and Owen, S. M.: Eddy flux and leaf-level measurements of biogenic VOC emissions from  
703 mopane woodland of Botswana, *J. Geophys. Res.*, 108, doi:10.1029/2002JD002317, 2003.

704 Greenberg, J., Guenther, A., Madronich, S., Baugh, W., Ginoux, P., Druilhet, A., Delmas, R. and  
705 Delon, C.: Biogenic volatile organic compound emissions in central Africa during the  
706 Experiment for the Regional Sources and Sinks of Oxidants (EXPRESSO) biomass burning  
707 season, *J. Geophys. Res.*, 104, 30659–30671, doi:10.1029/1999JD900475, 1999.

708 Grossmann, D., Moorgat, G. K., Kibler, M., Schlomski, S., Bächman, K., Alicke, B., Geyer, A.,  
709 Platt, U., Hammer, M.-U., Vogel, B., Mihelcic, A., Hofzumahaus, A., Holland, F. and Volz-  
710 Thomas, A.: Hydrogen peroxide, organic peroxides, carbonyl compounds, and organic acids  
711 measured at Pabstthum during BERLIOZ, *J. Geophys. Res.*, 108, doi:10.1029/2001JD001096,  
712 2003.

713 Guenther, A., Hewitt, C. N., Erickson, D., Fall, R., Geron, C., Graedel, T., Harley, P., Klinger, L.  
714 F., Lerdau, M., McKay, W., Pierce, T., Scholes, B., Steinbrecher, R., Tallamraju, R., Taylor, J.  
715 and Zimmerman, P.: A global model of natural volatile organic compound emissions, *J.*  
716 *Geophys. Res.*, 100, 8873–8892, doi:10.1029/94JD02950, 1995.

717 Guenther, A., Karl, T., Harley, P., Wiedinmyer, C., Palmer, P. I. and Geron, C.: Estimates of  
718 global terrestrial isoprene emissions using MEGAN (Model of Emissions of Gases and Aerosols  
719 from Nature), *Atmos. Chem. Phys.*, 6, 3181-3210, 2006.

720 Guenther, A., Otter, L. B., Zimmerman, P., Greenberg, J., Scholes, R. and Scholes, M.: Biogenic  
721 hydrocarbon emissions from southern African savannas, *J. Geophys. Res.*, 101, 25859-25865,  
722 doi:10.1029/96JD02597, 1996.

723 Hak, C., Pundt, I., Kern, C., Platt, U., Dommen, J., Ordóñez, C., Prévôt, A. S. H., Junkermann,  
724 W., Astorga-Lloréns, C., Larsen, B. R., Mellqvist, J., Strandberg, A., Yu, Y., Galle, B.,  
725 Kleffman, J., Lörzer, J. C., Braathen, G. O. and Volkamer, R.: Intercomparison of four different  
726 in-situ techniques for ambient formaldehyde measurements in urban air, *Atmos. Chem. Phys.*, 5,  
727 2881-2900, 2005.

728 Harley, P., Otter, L. B., Guenther, A. and Greenberg, J.: Micrometeorological and leaf-level  
729 measurements of isoprene emissions from a southern African savanna, *J. Geophys. Res.*, 108,  
730 doi:10.1029/2002JD002592, 2003.

- 731 Henze, D. K. and Seinfeld, J. H.: Global secondary organic aerosol from isoprene oxidation,  
732 *Geophys. Res. Lett.*, 33, doi:10.1029/2006GL025976, 2006.
- 733 Hobbs, P. V., Reid, J. S., Herring, J. A., Nance, J. D., E. Weiss, R., Ross, J. L., Hegg, D. A.,  
734 Ottmar, R. D. and Lioussé, C.: Particle and trace-gas measurements in the smoke from  
735 prescribed burns of forest products in the Pacific Northwest, in *Biomass Burning and Global  
736 Change*, edited by J. S. Levine, pp. 697–715, MIT Press, Cambridge, MA., 1996.
- 737 Hopkins, J., Evans, M. J., Lee, J. D., Lewis, A. C., Marsham, J. H., McQuaid, J. B., Parker, D. J.,  
738 Stewart, D. J., Reeves, C. E. and Purvis, R. M.: Direct estimates of emissions from the megacity  
739 of Lagos, *Atmos. Chem. Phys.*, 9, 8471-8477, 2009.
- 740 Horowitz, L. W., Liang, J., Gardner, G. M. and Jacob, D. J.: Export of reactive nitrogen from  
741 North America during summertime: Sensitivity to hydrocarbon chemistry, *J. Geophys. Res.*, 103,  
742 13451-13476, doi:10.1029/97JD03142, 1998.
- 743 Jaeglé, L., Steinberger, L., Martin, R. V. and Chance, K.: Global partitioning of NO<sub>x</sub> sources  
744 using satellite observations: Relative roles of fossil fuel combustion, biomass burning and soil  
745 emissions, *Faraday Discuss.*, 130, 407-423, 2005.
- 746 Janicot, S., Thorncroft, C. D., Ali, A., Asencio, N., Berry, G., Bock, O., Bourles, B., Caniaux,  
747 G., Chauvin, F., Deme, A., Kergoat, L., Lafore, J.-P., Lavaysse, C., Lebel, T., Marticorena, B.,  
748 Mounier, F., Nedelec, P., Redelsperger, J.-L., Ravegnani, F., Reeves, C. E., Roca, R., de Rosnay,  
749 P., Schlager, H., Sultan, B., Tomasini, M. and Ulanovsky, A.: Large-scale overview of the  
750 summer monsoon over West Africa during the AMMA field experiment in 2006, *Ann. Geophys.*,  
751 26, 2569-2595, 2008.
- 752 Karl, T., Guenther, A., Turnipseed, A., Tyndall, G., Artaxo, P. and Martin, S.: Rapid formation  
753 of isoprene photo-oxidation products observed in Amazonia, *Atmos. Chem. Phys.*, 9, 7753-7767,  
754 2009.
- 755 Karl, T., Harley, P., Emmons, L., Thornton, B., Guenther, A., Basu, C., Turnipseed, A. and  
756 Jardine, K.: Efficient atmospheric cleansing of oxidized organic trace gases by vegetation,  
757 *Science*, 330, 816-819, 2010.
- 758 Karl, T., Potosnak, M., Guenther, A., Clark, D., Walker, J., Herrick, J. D. and Geron, C.:  
759 Exchange processes of volatile organic compounds above a tropical rain forest: Implications for  
760 modeling tropospheric chemistry above dense vegetation, *J. Geophys. Res.*, 109,  
761 doi:10.1029/2004JD004738, 2004.
- 762 Kim, J. H., Kim, S. M., Baek, K. H., Wang, L., Kurosu, T. P., De Smedt, I., Chance, K. and  
763 Newchurch, M. J.: Evaluation of satellite-derived HCHO using statistical methods, *Atmos.  
764 Chem. Phys.*, 11, 8003-8025, 2011.
- 765 Kleipool, Q. L., Dobber, M. R., de Haan, J. F. and Levelt, P. F.: Earth surface reflectance  
766 climatology from 3 years of OMI data, *J. Geophys. Res.*, 113, doi:10.1029/2008JD010290, 2008.

767 Klemp, D., Mannschreck, K. and Mittermaier, B.: Comparison of two different HCHO  
768 Measurement Techniques: TDLAS and a commercial Hantzsch Monitor – Results from Long  
769 term Measurements in a City Plume during the EVA Experiment, in Emissions of Air Pollutants  
770 – Measurements, Calculations and Uncertainties, edited by R. Friedrich and S. Reis, Springer  
771 Verlag., 2003.

772 Klinger, L. F., Guenther, G., Tyndall, G., Zimmerman, P., Bangui, M. M., Moutsamboté, J.-M.  
773 and Kenfack, D.: Patterns in volatile organic compound emissions along a savanna-rainforest  
774 gradient in central Africa, *J. Geophys. Res.*, 103, 1443-1454, doi:10.1029/97JD02928, 1998.

775 Koelemeijer, R. B. A. and Stammes, P.: Validation of Global Ozone Monitoring Experiment  
776 cloud fractions relevant for accurate ozone column retrieval, *J. Geophys. Res.*, 104, 18801-  
777 18814, doi:10.1029/1999JD900279, 1999.

778 Koster, R. D., Suarez, M. J., Ducharne, A., Stieglitz, M. and Kumar, P.: A catchment-based  
779 approach to modeling land surface processes in a general circulation model 1. Model structure, *J.*  
780 *Geophys. Res.*, 105, 24809-24822, doi:10.1029/2000JD900327, 2000.

781 Kroll, J. H., Ng, N. L., Murphy, S. M., Flagan, R. C. and Seinfeld, J. H.: Secondary Organic  
782 Aerosol Formation from Isoprene Photooxidation, *Environ. Sci. Technol.*, 40, 1869-1877, 2006.

783 Lelieveld, J., Butler, T. M., Crowley, J. N., Dillon, T. J., Fischer, H., Ganzeveld, L., Harder, H.,  
784 Lawrence, M. G., Martinez, M., Taraborrelli, D. and Williams, J.: Atmospheric oxidation  
785 capacity sustained by a tropical forest, *Nature*, 452, 737-740, 2008.

786 Levelt, P. F., van den Oord, G. H. J., Dobber, M. R., Malkki, A., Stammes, P., Lundell, J. O. V.  
787 and Saari, H.: The ozone monitoring instrument, *IEEE T. Geosci. Remote Sens.*, 44, 1093-1101,  
788 2006.

789 Manly, B. F. J.: Randomization, bootstrap and Monte Carlo methods in biology, Chapman and  
790 Hall, New York., 1997.

791 Mao, J., Jacob, D. J., Evans, M. J., Olson, J. R., Ren, X., Brune, W. H., Clair, J. M. S., Crouse,  
792 J. D., Spencer, K. M., Beaver, M. R., Wennberg, P. O., Cubison, M. J., Jimenez, J. L., Fried, A.,  
793 Weibring, P., Walega, J. G., Hall, S. R., Weinheimer, a. J., Cohen, R. C., Chen, G., Crawford, J.  
794 H., McNaughton, C., Clarke, a. D., Jaeglé, L., Fisher, J. a., Yantosca, R., Le Sager, P. and  
795 Carouge, C.: Chemistry of hydrogen oxide radicals ( $\text{HO}_x$ ) in the Arctic troposphere in spring,  
796 *Atmos. Chem. Phys.*, 10, 5823-5838, 2010.

797 Mari, C. H., Cailley, G., Corre, L., Saunois, M., Attié, J. L., Thouret, V. and Stohl, A.: Tracing  
798 biomass burning plumes from the Southern Hemisphere during the AMMA 2006 wet season  
799 experiment, *Atmos. Chem. Phys.*, 8, 3951-3961, 2008.

800 Meyer-Arne, J., Ladstätter-Weissenmayer, A., Richter, A., Wittrock, F. and Burrows, J. P.: A  
801 study of the trace gas columns of  $\text{O}_3$ ,  $\text{NO}_2$  and HCHO over Africa in September 1997, *Faraday*  
802 *Discuss.*, 130, 387-405, 2005.

803 Millet, D. B., Jacob, D. J., Boersma, K., Fu, T.-M., Kurosu, T. P., Chance, K., Heald, C. L. and  
804 Guenther, A.: Spatial distribution of isoprene emissions from North America derived from  
805 formaldehyde column measurements by the OMI satellite sensor, *J. Geophys. Res.*, 113,  
806 doi:10.1029/2007JD008950, 2008.

807 Millet, D. B., Jacob, D. J., Turquety, S., Hudman, R. C., Wu, S., Fried, A., Walega, J. G., Heikes,  
808 B. G., Blake, D. R., Singh, H. B., Anderson, B. E. and Clarke, A. D.: Formaldehyde distribution  
809 over North America: Implications for satellite retrievals of formaldehyde columns and isoprene  
810 emission, *J. Geophys. Res.*, 111, doi:10.1029/2005JD006853, 2006.

811 Misztal, P. K., Owen, S. M., Guenther, A., Rasmussen, R., Geron, C., Harley, P., Phillips, G. J.,  
812 Ryan, A., Edwards, D. P., Hewitt, C. N., Nemitz, E., Siong, J., Heal, M. R. and Cape, J. N.:  
813 Large estragole fluxes from oil palms in Borneo, *Atmos. Chem. Phys.*, 10, 4343-4358, 2010.

814 Moore, D. P. and Remedios, J. J.: Seasonality of Peroxyacetyl nitrate (PAN) in the upper  
815 troposphere and lower stratosphere using the MIPAS-E instrument, *Atmos. Chem. Phys.*, 10(13),  
816 6117-6128, doi:10.5194/acp-10-6117-2010, 2010.

817 Murphy, J. G., Oram, D. E. and Reeves, C. E.: Measurements of volatile organic compounds  
818 over West Africa, *Atmos. Chem. Phys.*, 10, 5281-5294, 2010.

819 Müller, J.F., Stavrou, T., Wallens, S., De Smedt, I., Van Roozendaal, M., Potosnak, M., Rinne,  
820 J., Munger, B., Goldstein, A. and Guenther, A.: Global isoprene emissions estimated using  
821 MEGAN, ECMWF analyses and a detailed canopy environment model, *Atmos. Chem. Phys.*, 8,  
822 1329-1341, 2008.

823 Oketola, A. A. and Osibanjo, O.: Estimating sectoral pollution load in Lagos by Industrial  
824 Pollution Projection System (IPPS), *Sci. Total Environ.*, 377, 125-141, 2007.

825 Olivier JGJ, Bouwman AF, Maas CWM van der, Berdowski JJM, Veldt C, Bloos JPJ,  
826 Visschedijk AJH, Zandveld PYJ, H. J.: Description of EDGAR Version 2.0: A set of global  
827 emission inventories of greenhouse gases and ozone-depleting substances for all anthropogenic  
828 and most natural sources on a per country basis and on 1 degree x 1 degree grid, Bilthoven, The  
829 Netherlands., 1996.

830 Olson, D. M., Dinerstein, E., Wikramanayake, E. D., Burgess, N. D., Powell, G. V. N.,  
831 Underwood, E. C., D'amico, J. A., Itoua, I., Strand, H. E., Morrison, J. C., Loucks, C. J., Allnutt,  
832 T. F., Ricketts, T. H., Kura, Y., Lamoreux, J. F., Wettengel, W. W., Hedao, P. and Kassem, K. R.:  
833 Terrestrial ecoregions of the world: a new map of life on earth, *BioScience*, 51, 933-938, 2001.

834 Otter, L. B., Guenther, A. and Greenberg, J.: Seasonal and spatial variations in biogenic  
835 hydrocarbon emissions from southern African savannas and woodlands, *Atmos. Environ.*, 36,  
836 4265-4275, 2002.

837 Otter, L. B., Guenther, A., Wiedinmyer, C., Fleming, G., Harley, P. and Greenberg, J.: Spatial  
838 and temporal variations in biogenic volatile organic compound emissions for Africa south of the  
839 equator, *J. Geophys. Res.*, 108, doi:10.1029/2002JD002609, 2003.

840 Palmer, P. I., Abbot, D. S., Fu, T.-M., Jacob, D. J., Chance, K., Kurosu, T. P., Guenther, A.,  
841 Wiedinmyer, C., Stanton, J., Pilling, M., Pressley, S. N., Lamb, B. and Sumner, A. L.:  
842 Quantifying the seasonal and interannual variability of North American isoprene emissions using  
843 satellite observations of the formaldehyde column, *J. Geophys. Res.*, 111,  
844 doi:10.1029/2005JD006689, 2006.

845 Palmer, P. I., Jacob, D. J., Fiore, A., Martin, R. V., Chance, K. and Kurosu, T. P.: Mapping  
846 isoprene emissions over North America using formaldehyde column observations from space, *J.*  
847 *Geophys. Res.*, 108, doi:10.1029/2002JD002153, 2003.

848 Palmer, P. I., Jacob, D. J., Martin, R. V., Bey, I., Yantosca, R., Fiore, A., Li, Q., Chance, K.,  
849 Spurr, R. J. D. and Kurosu, T. P.: Air mass factor formulation for spectroscopic measurements  
850 from satellites- Application to formaldehyde retrievals from the Global Ozone Monitoring  
851 Experiment, *J. Geophys. Res.*, 106, 14539–14550, doi:10.1029/2000JD900772, 2001.

852 Park, R. J., Jacob, D. J., Field, B. D., Yantosca, R. and Chin, M.: Natural and transboundary  
853 pollution influences on sulfate-nitrate-ammonium aerosols in the United States: Implications for  
854 policy, *J. Geophys. Res.*, 109, doi:10.1029/2003JD004473, 2004.

855 Paulot, F., Crounse, J. D., Kjaergaard, H. G., Kroll, J. H., Seinfeld, J. H. and Wennberg, P. O.:  
856 Isoprene photooxidation: new insights into the production of acids and organic nitrates, *Atmos.*  
857 *Chem. Phys.*, 9, 1479-1501, 2009a.

858 Paulot, F., Crounse, J. D., Kjaergaard, H. G., Kürten, A., St Clair, J. M., Seinfeld, J. H. and  
859 Wennberg, P. O.: Unexpected epoxide formation in the gas-phase photooxidation of isoprene,  
860 *Science*, 325, 730-733, 2009b.

861 Paulson, S. E., Flagan, R. C. and Seinfeld, J. H.: Atmospheric photooxidation of isoprene part I:  
862 The hydroxyl radical and ground state atomic oxygen reactions, *Int. J. Chem. Kinet.*, 24, 79-101,  
863 1992.

864 Peeters, J. and Müller, J.-F.: HOx radical regeneration in isoprene oxidation via peroxy radical  
865 isomerisations. II: experimental evidence and global impact, *Phys. Chem. Chem. Phys.*, 12,  
866 14227-14335, 2010.

867 Peeters, J., Nguyen, T. L. and Vereecken, L.: HOx radical regeneration in the oxidation of  
868 isoprene, *Phys. Chem. Chem. Phys.*, 11, 5935-5939, 2009.

869 Pugh, T. A. M., MacKenzie, A. R., Hewitt, C. N., Langford, B., Edwards, P. M., Furneaux, K.  
870 L., Heard, D. E., Hopkins, J. R., Jones, C. E., Karunaharan, A., Lee, J., Mills, G., Misztal, P. K.,  
871 Moller, S., Monks, P. S. and Whalley, L. K.: Simulating atmospheric composition over a South-

- 872 East Asian tropical rainforest: performance of a chemistry box model, *Atmos. Chem. Phys.*, 10,  
873 279-298, 2010.
- 874 Redelsperger, J.-L., Thorncroft, C. D., Diedhiou, A., Lebel, T., Parker, D. J. and Polcher, J.:  
875 African Monsoon Multidisciplinary Analysis (AMMA): An international research project and  
876 field campaign, *B. Am. Meteorol. Soc.*, 87, 1739–1746, 2006.
- 877 Reeves, C. E., Formenti, P., Afif, C., Ancellet, G., Attié, J. L., Bechara, J., Borbon, A., Cairo, F.,  
878 Coe, H., Crumeyrolle, S., Fierli, F., Flamant, C., Gomes, L., Hamburger, T., Jambert, C., Law,  
879 K. S., Mari, C. H., Jones, R. L., Matsuki, A., Mead, M. I., Methven, J., Mills, G., Minikin, A.,  
880 Murphy, J. G., Nielsen, J. K., Oram, D. E., Parker, D. J., Richter, A., Schlager, H.,  
881 Schwarzenboeck, A. and Thouret, V.: Chemical and aerosol characterisation of the troposphere  
882 over West Africa during the monsoon period as part of AMMA, *Atmos. Chem. Phys.*, 10, 7575-  
883 7601, 2010.
- 884 Ren, X., Olson, J. R., Crawford, J. H., Brune, W. H., Mao, J., Long, R. B., Chen, Z., Chen, G.,  
885 Avery, M. a., Sachse, G. W., Barrick, J. D., Diskin, G. S., Huey, G., Fried, A., Cohen, R. C.,  
886 Heikes, B., Wennberg, P. O., Singh, H. B., Blake, D. R. and Shetter, R. E.: HO<sub>x</sub> chemistry during  
887 INTEX-A 2004: Observation, model calculation, and comparison with previous studies, *J.*  
888 *Geophys. Res.*, 113, doi:10.1029/2007JD009166, 2008.
- 889 Saunders, S. M., Jenkin, M. E., Derwent, R. G. and Pilling, M. J.: Protocol for the development  
890 of the Master Chemical Mechanism, MCM v3 (Part A): tropospheric degradation of non-  
891 aromatic volatile organic compounds, *Atmos. Chem. Phys.*, 3, 161–180, 2003.
- 892 Saxton, J. E., Lewis, A. C., Kettlewell, J. H., Ozel, M. Z., Gogus, F., Boni, Y., Korogone, S. O.  
893 U. and Serça, D.: Isoprene and monoterpene measurements in a secondary forest in northern  
894 Benin, *Atmos. Chem. Phys.*, 7, 4095-4106, 2007.
- 895 Serça, D., Guenther, A., Klinger, L. F., Vierling, L., Harley, P., Druilhet, A., Greenberg, J.,  
896 Baker, B., Baugh, W., BOUKA-BIONA, C. and Loemba-Ndembi, J.: EXPRESSO flux  
897 measurements at upland and lowland Congo tropical forest site, *Tellus B*, 53, 220–234, 2001.
- 898 Shim, C., Wang, Y., Choi, Y., Palmer, P. I., Abbot, D. S. and Chance, K.: Constraining global  
899 isoprene emissions with Global Ozone Monitoring Experiment (GOME) formaldehyde column  
900 measurements, *J. Geophys. Res.*, 110, doi:10.1029/2004JD005629, 2005.
- 901 Singh, H. B. and Hanst, P. L.: Peroxyacetyl nitrate (PAN) in the unpolluted atmosphere,  
902 *Geophys. Res. Lett.*, 8(8), 941-944, 1981.
- 903 de Smedt, I., Müller, J.-F., Stavrou, T., van der A, R., Eskes, H. and Van Roozendaal, M.:  
904 Twelve years of global observations of formaldehyde in the troposphere using GOME and  
905 SCIAMACHY sensors, *Atmos. Chem. Phys.*, 8, 4947-4963, 2008.
- 906 South African Petroleum Industry Association: Annual Report 2008., 2008.

- 907 Spurr, R. J. D., Kurosu, T. P. and Chance, K.: A linearized discrete ordinate radiative transfer  
908 model for atmospheric remote-sensing retrieval, *J. Quant. Spectrosc. Ra.*, 68, 689–735, 2001.
- 909 Stammes, P., Sneep, M., de Haan, J. F., Veefkind, J. P., Wang, P. and Levelt, P. F.: Effective  
910 cloud fractions from the Ozone Monitoring Instrument: Theoretical framework and validation, *J.*  
911 *Geophys. Res.*, 113, doi:10.1029/2007JD008820, 2008.
- 912 Stavrakou, T., Müller, J., De Smedt, I., Van Roozendael, M., Van Der Werf, G. R., Giglio, L.  
913 and Guenther, A.: Global emissions of non-methane hydrocarbons deduced from SCIAMACHY  
914 formaldehyde columns through 2003-2006, *Atmos. Chem. Phys.*, 9, 3663–3679, 2009a.
- 915 Stavrakou, T., Müller, J.-F., De Smedt, I., Van Roozendael, M., Van Der Werf, G. R., Giglio, L.  
916 and Guenther, A.: Evaluating the performance of pyrogenic and biogenic emission inventories  
917 against one decade of space-based formaldehyde, *Atmos. Chem. Phys.*, 9, 1037–1060, 2009b.
- 918 Stewart, D. J., Taylor, C., Reeves, C. E. and McQuaid, J. B.: Biogenic nitrogen oxide emissions  
919 from soils: impact on NO<sub>x</sub> and ozone over west Africa during AMMA (African Monsoon  
920 Multidisciplinary Analysis) observational, *Atmos. Chem. Phys.*, 8, 2285-2297, 2008.
- 921 Still, T. J., Al-Haider, S., Seakins, P. W., Sommariva, R., Stanton, J. C., Mills, G. and Penkett, S.  
922 A.: Ambient formaldehyde measurements made at a remote marine boundary layer site during  
923 the NAMBLEX campaign - a comparison of data from chromatographic and modified Hantzsch  
924 techniques, *Atmos. Chem. Phys.*, 6, 2711–2726, 2006.
- 925 Stone, D., Evans, M. J., Commane, R., Ingham, T., Floquet, C. F. a., McQuaid, J. B., Brookes,  
926 D. M., Monks, P. S., Purvis, R. M., Hamilton, J. F., Hopkins, J., Lee, J. D., Lewis, a. C., Stewart,  
927 D. J., Murphy, J. G., Mills, G., Oram, D. E., Reeves, C. E. and Heard, D. E.: HO<sub>x</sub> observations  
928 over West Africa during AMMA: impact of isoprene and NO<sub>x</sub>, *Atmos. Chem. Phys.*, 10, 9415-  
929 9429, 2010.
- 930 Sumner, A. L., Shepson, P. B., Couch, T. L., Thornberry, T., Carroll, M. A., Sillman, S., Pippin,  
931 M., Bertman, S., Tan, D., Faloon, I., Brune, W., Young, V., Cooper, O., Moody, J. and  
932 Stockwell, W.: A study of formaldehyde chemistry above a forest canopy, *J. Geophys. Res.*, 106,  
933 24387–24405, doi:10.1029/2000JD900761, 2001.
- 934 Tao, Z., Larson, S. M., Wuebbles, D. J., Williams, A. and Caughey, M.: A summer simulation of  
935 biogenic contributions to ground-level ozone over the continental United States, *J. Geophys.*  
936 *Res.*, 108, doi:10.1029/2002JD002945, 2003.
- 937 Torres, O., Tanskanen, A., Veihelmann, B., Ahn, C., Braak, R., Bhartia, P. K., Veefkind, J. P.  
938 and Levelt, P. F.: Aerosols and surface UV products from Ozone Monitoring Instrument  
939 observations: An overview, *J. Geophys. Res.*, 112, doi:10.1029/2007JD008809, 2007.
- 940 Trainer, M., Williams, E. J., Parrish, D. D., Buhr, M. P., Allwine, E. J., Westberg, H. H.,  
941 Fehsenfeld, F. C. and Liu, S. C.: Models and observations of the impact of natural hydrocarbons  
942 on rural ozone, *Nature*, 329, 705-707, 1987.

943 Trentmann, J., Andreae, M. O. and Graf, H.-F.: Chemical processes in a young biomass-burning  
944 plume, *J. Geophys. Res.*, 108, doi:10.1029/2003JD003732, 2003.

945 US EPA: Estimation Programs Interface for Windows Vista v4.10, US EPA., 2011.

946 Wang, Y., Jacob, D. J. and Logan, J. A.: Global simulation of tropospheric O<sub>3</sub>-NO<sub>x</sub>-hydrocarbon  
947 chemistry. 1. Model formulation, *J. Geophys. Res.*, 103, 10713-10725, doi:10.1029/98JD00158,  
948 1998.

949 Van der Werf, G. R., Randerson, J. T., Giglio, L., Collatz, G. J., Kasibhatla, P. S. and Arellano,  
950 A. F.: Interannual variability of global biomass burning emissions from 1997 to 2004, *Atmos.*  
951 *Chem. Phys.*, 6, 3423-3441, 2006.

952 Wesely, M.: Parameterization of surface resistances to gaseous dry deposition in regional-scale  
953 numerical models, *Atmos. Environ.*, 23, 1293–1304, 1989.

954 Yang, W., Shabanov, N. V., Huang, D., Wang, W., Dickinson, R. E., Nemani, R. R.,  
955 Knyazikhin, Y. and Myneni, R. B.: Analysis of leaf area index products from combination of  
956 MODIS Terra and Aqua data, *Remote Sens. Environ.*, 104, 297-312, 2006.

957 Yevich, R. and Logan, J. A.: An assessment of biofuel use and burning of agricultural waste in  
958 the developing world, *Global Biogeochem. Cy.*, 17, doi:10.1029/2002GB001952, 2003.

959 Yienger, J. and Levy II, H.: Empirical model of global soil-biogenic NO<sub>x</sub> emissions, *J. Geophys.*  
960 *Res.*, 100, 11447–11464, doi:10.1029/95JD00370, 1995.

961 Zeng, X.: Global vegetation root distribution for land modeling, *J. Hydrometeorol.*, 2, 525–530,  
962 2001.

963

964 **Figure Captions**

965 Figure 1:

966 HCHO columns and land cover types over Africa. The first three panels are annual mean HCHO  
967 columns for 2005-2009 at  $1^\circ \times 1^\circ$  resolution: (a) original slant columns, (b) biogenic slant  
968 columns after removing biomass burning, dust, and anthropogenic influences, (c) vertical  
969 columns obtained by applying air mass factors (AMFs) to the slant columns. The bottom right  
970 panel (d) shows the Global Land Cover (GLC) map for 2000 (Bartholomé and Belward, 2005).

971

972 Figure 2:

973 Cumulative probability distribution of OMI smoke AAOD 8-day average values at  $1^\circ \times 1^\circ$   
974 resolution over southern Africa (south of  $2^\circ\text{S}$ ) for 2005-2009. The  $x$ -axis is a probability scale  
975 such that a normal distribution would plot as a straight line. This allows us to separate biomass  
976 burning from non-biomass burning conditions by plotting separate regression lines fitted to the  
977 bottom and top quantiles of the data. Intersection of these regression lines defines a smoke  
978 AAOD threshold for diagnosing biomass burning conditions and we remove the corresponding  
979 scenes from the OMI data set. Different AAOD thresholds are used for different regions of  
980 Africa as discussed in the text.

981

982 Figure 3:

983 Flow chart of the filtering algorithm used to remove biomass burning, dust, and anthropogenic  
984 influences in OMI slant HCHO columns ( $\Omega_s$ ). All data are 8-day averages on the same  $1^\circ \times 1^\circ$   
985 grid. The MODIS fire counts filter uses MODIS data for the 8-day periods preceding and  
986 concurrent with the OMI HCHO observation.

987 Figure 4:  
988 Cumulative yields of HCHO per unit carbon from isoprene oxidation as a function of time in the  
989 DSMACC chemistry box model using the standard GEOS-Chem chemistry scheme (red) and the  
990 Paulot scheme (blue) for different NO<sub>x</sub> levels and initialized at local noon. Details on the box  
991 model simulation are given in the text.

992  
993 Figure 5:  
994 Mean latitudinal gradients of boundary layer (>900 hPa) isoprene, MVK+MACR, and HCHO  
995 concentrations during the AMMA aircraft campaign in July-August 2006. The left panel shows  
996 the AMMA flight tracks superimposed on a map of MODIS leaf area index (LAI) (Yang et al.,  
997 2006) for the AMMA period. Observations averaged over 0.5° latitudinal bins are shown in  
998 black. Model results sampled along the flight tracks and at the flight times are shown in red  
999 (standard GEOS-Chem isoprene oxidation scheme) and in blue (Paulot scheme). Mean OMI  
1000 HCHO for July-August 2005-2009 is shown in orange (see text).

1001  
1002 Figure 6:  
1003 Annual mean tropospheric NO<sub>2</sub> columns over Africa at 12-15 local time (LT). The left panel  
1004 shows OMI 2005-2009 data at 1°×1° resolution (Boersma et al., 2007). The right panel shows  
1005 GEOS-Chem model values for 2006. The colorbar includes boundary layer (i.e. below 900 hPa)  
1006 NO<sub>x</sub> estimated from column NO<sub>2</sub> (see text for details). Biomass burning influence was removed  
1007 using MODIS fire counts and OMI smoke AAOD in the observations, and BC AOD in GEOS-  
1008 Chem. The equator is indicated.

1009

1010 Figure 7:  
1011 Mean longitudinal gradients of isoprene emission (black) and HCHO columns (color) across  
1012 central Africa (3°S-3°N) at 12-15 LT in July. HCHO columns are shown for the OMI  
1013 observations in 2005-2009 (orange) and from the GEOS-Chem simulations using the standard  
1014 isoprene oxidation scheme (red) and the Paulot scheme (blue) in 2006 at 12-15 LT. Isoprene  
1015 emissions are from MEGAN. The HCHO columns have been filtered against biomass burning as  
1016 described in the text.

1017

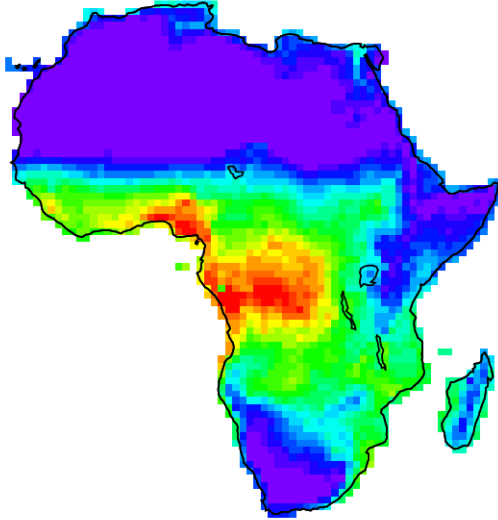
1018 Figure 8:  
1019 Dependence of the HCHO-isoprene relationship on the local tropospheric NO<sub>2</sub> column  $\Omega_{\text{NO}_2}$   
1020 over Africa in GEOS-Chem. The figure shows statistics of  $S = \Delta\Omega_{\text{HCHO}}/\Delta E_{\text{ISOP}}$  computed as  
1021 described in the text for individual 2°×2.5° gridsquares and months in 2006 at 12-15 LT. Values  
1022 of  $S$  have been sorted by the local value of  $\Omega_{\text{NO}_2}$  in  $1 \times 10^{14}$  molecules cm<sup>-2</sup> bins, and means and  
1023 standard deviations are shown in each bin for GEOS-Chem using the standard isoprene oxidation  
1024 scheme (red) and the Paulot scheme (blue). The data for  $\Omega_{\text{NO}_2} \leq 1 \times 10^{15}$  molecules cm<sup>-2</sup> show a  
1025 linear relationship between  $S$  and  $\Omega_{\text{NO}_2}$ , and reduced-major-axis regression parameters are shown  
1026 inset with standard deviations determined using jackknife resampling (Manly, 1997). The data  
1027 for  $\Omega_{\text{NO}_2} > 1 \times 10^{15}$  molecules cm<sup>-2</sup> show no significant dependence between  $S$  and  $\Omega_{\text{NO}_2}$ , and the  
1028 corresponding mean values and standard deviations of  $S$  are shown inset. The mean  $\Omega_{\text{NO}_2}$   
1029 inferred from AMMA observations is also indicated (orange arrow).

1030

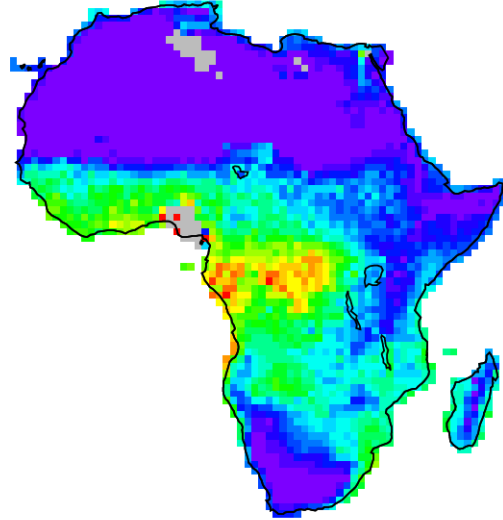
1031 Figure 9:

1032 Annual average isoprene emissions from Africa at  $1^{\circ}\times 1^{\circ}$  horizontal resolution at 12-15 LT.  
1033 Values inferred from the OMI HCHO 2005-2009 data (left) are compared to values from the  
1034 MEGAN bottom-up inventory (center). The right panel shows the difference between the two.  
1035 Results are for the ensemble of  $1^{\circ}\times 1^{\circ}$  gridsquare-months that are not excluded from our analysis  
1036 due to biomass burning, anthropogenic, dust, or smearing influences (see text). Completely  
1037 excluded areas are shown in grey.  
1038

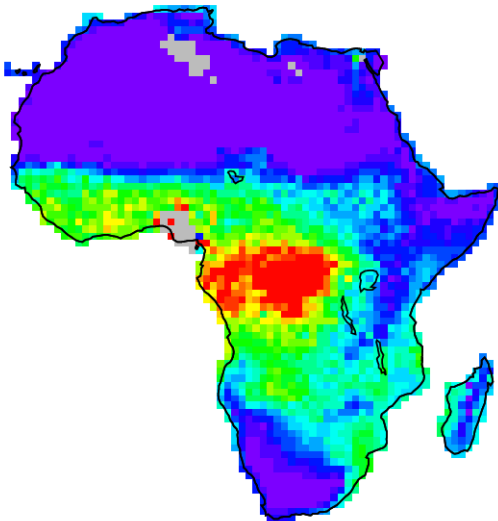
a. OMI HCHO slant columns  
original data



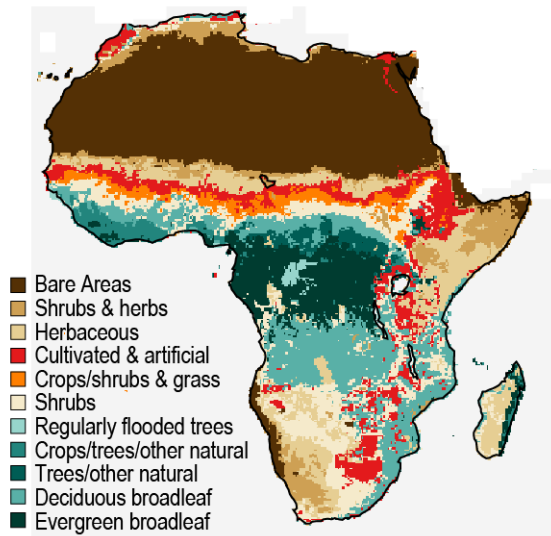
b. OMI HCHO slant columns  
biogenic component only



c. OMI HCHO vertical columns  
biogenic component only



d. GLC 2000 land cover



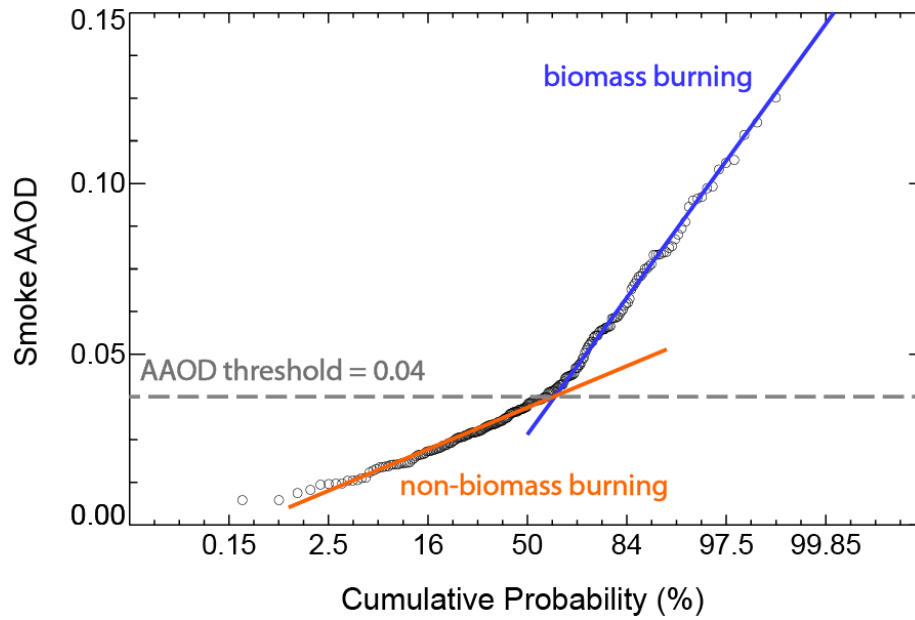
1040

1041 Figure 1: HCHO columns and land cover types over Africa. The first three panels are annual

1042 mean HCHO columns for 2005-2009 at  $1^\circ \times 1^\circ$  resolution: (a) original slant columns,

1043 (b) biogenic slant columns after removing biomass burning, dust, and anthropogenic

1044 influences, (c) vertical columns obtained by applying air mass factors (AMFs) to the  
1045 slant columns. The bottom right panel (d) shows the Global Land Cover (GLC) map  
1046 for 2000 (Bartholomé and Belward, 2005).  
1047



1048

1049

1050 Figure 2. Cumulative probability distribution of OMI smoke AAOD 8-day average values at

1051  $1^{\circ} \times 1^{\circ}$  resolution over southern Africa (south of  $2^{\circ}\text{S}$ ) for 2005-2009. The  $x$ -axis is a

1052 probability scale such that a normal distribution would plot as a straight line. This

1053 allows us to separate biomass burning from non-biomass burning conditions by

1054 plotting separate regression lines fitted to the bottom and top quantiles of the data.

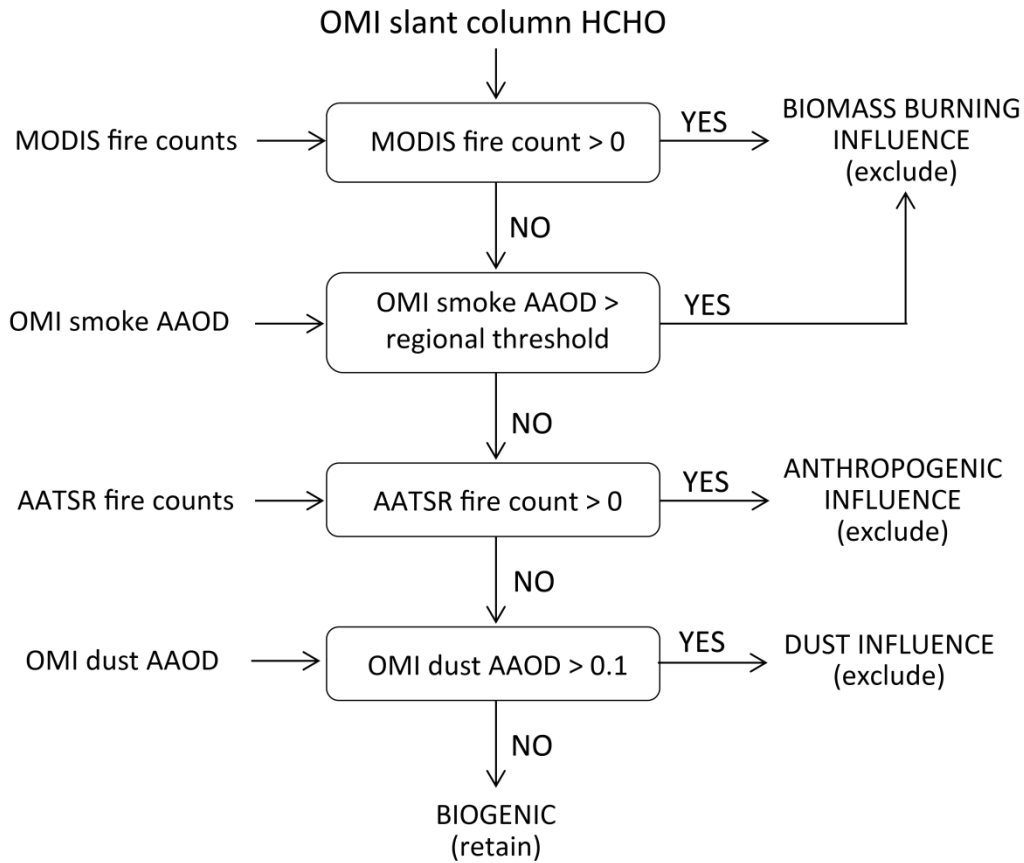
1055 Intersection of these regression lines defines a smoke AAOD threshold for diagnosing

1056 biomass burning conditions and we remove the corresponding scenes from the OMI

1057 data set. Different AAOD thresholds are used for different regions of Africa as

1058 discussed in the text.

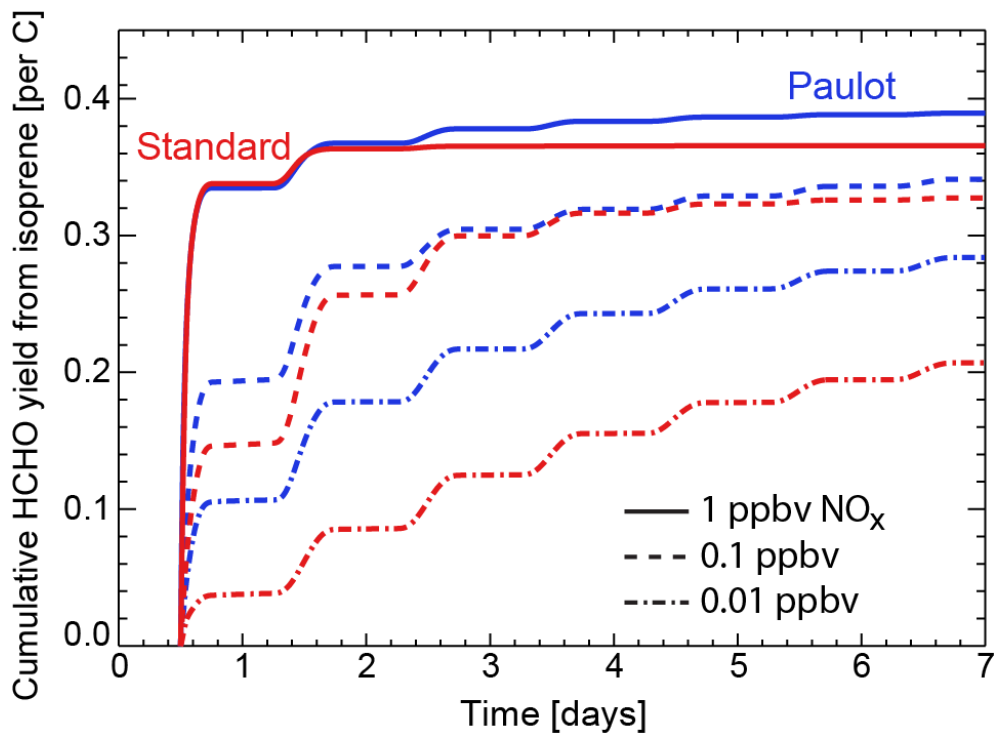
1059



1060

1061 Figure 3: Flow chart of the filtering algorithm used to remove biomass burning, dust, and  
 1062 anthropogenic influences in OMI slant HCHO columns ( $\Omega_s$ ). All data are 8-day  
 1063 averages on the same  $1^\circ \times 1^\circ$  grid. The MODIS fire counts filter uses MODIS data for  
 1064 the 8-day periods preceding and concurrent with the OMI HCHO observation.

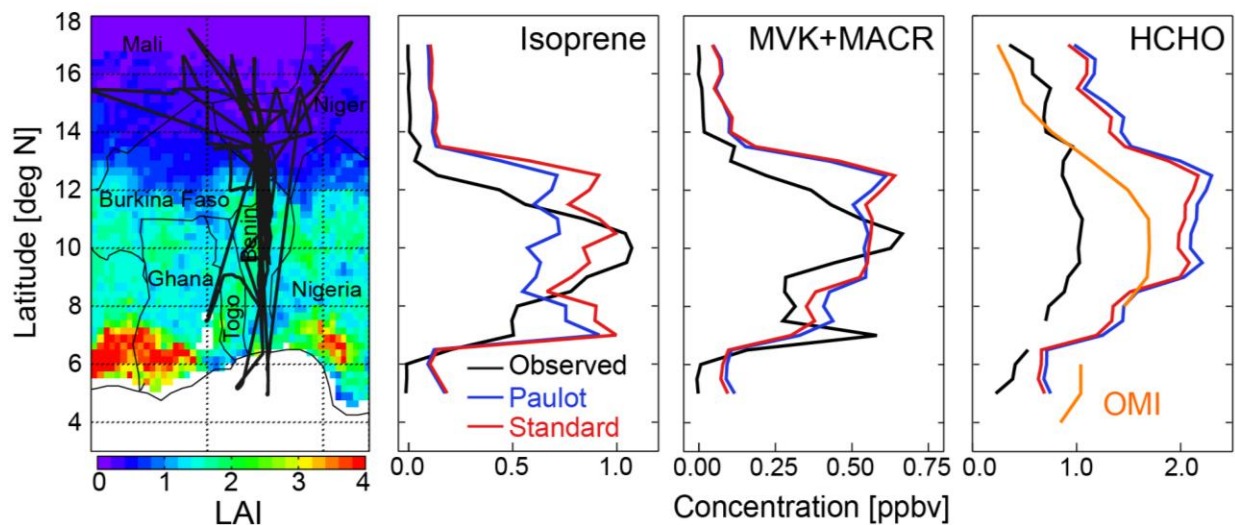
1065



1066

1067 Figure 4. Cumulative yields of HCHO per unit carbon from isoprene oxidation as a function of  
 1068 time in the DSMACC chemistry box model using the standard GEOS-Chem  
 1069 chemistry scheme (red) and the Paulot scheme (blue) for different NO<sub>x</sub> levels and  
 1070 initialized at local noon. Details on the box model simulation are given in the text.

1071



1072

1073 Figure 5. Mean latitudinal gradients of boundary layer (>900 hPa) isoprene, MVK+MACR,

1074 and HCHO concentrations during the AMMA aircraft campaign in July-August 2006.

1075 The left panel shows the AMMA flight tracks superimposed on a map of MODIS leaf

1076 area index (LAI) (Yang et al., 2006) for the AMMA period. Observations averaged

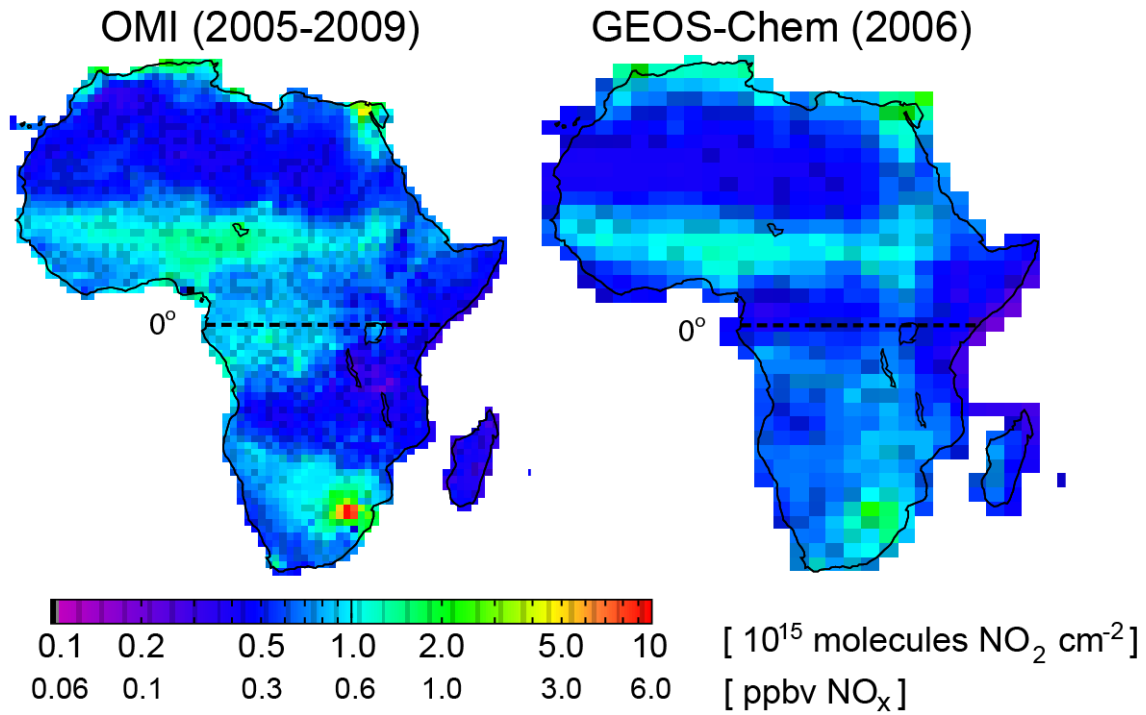
1077 over 0.5° latitudinal bins are shown in black. Model results sampled along the flight

1078 tracks and at the flight times are shown in red (standard GEOS-Chem isoprene

1079 oxidation scheme) and in blue (Paulot scheme). Mean OMI HCHO for July-August

1080 2005-2009 is shown in orange (see text).

1081



1082

1083

Figure 6. Annual mean tropospheric NO<sub>2</sub> columns over Africa at 12-15 local time (LT). The

1084

left panel shows OMI 2005-2009 data at 1°×1° resolution (Boersma et al., 2007).

1085

The right panel shows GEOS-Chem model values for 2006. The colorbar includes

1086

boundary layer NO<sub>x</sub> estimated from column NO<sub>2</sub> (see text for details). Biomass

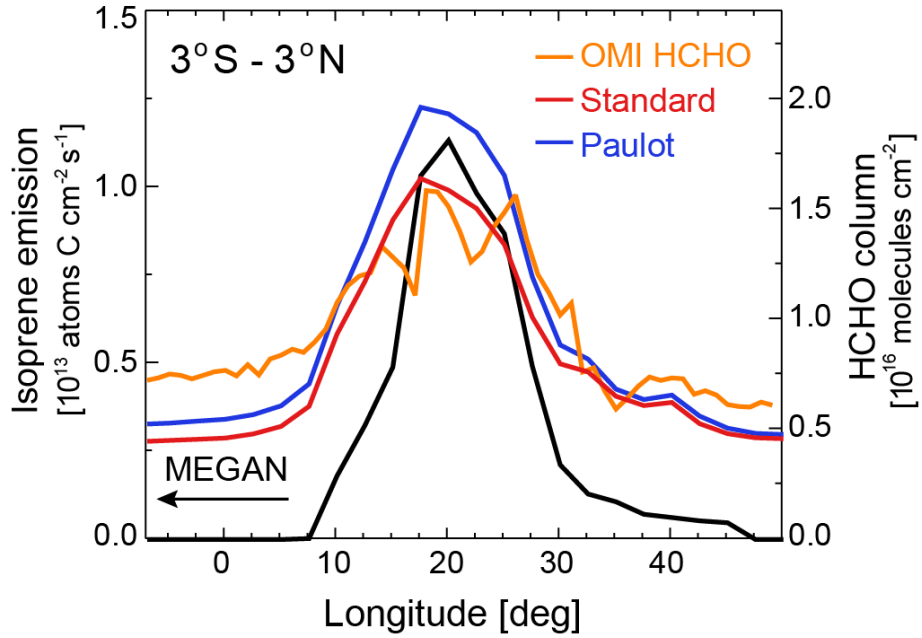
1087

burning influence was removed using MODIS fire counts and OMI smoke AAOD in

1088

the observations, and black carbon AOD in GEOS-Chem. The equator is indicated.

1089



1090

1091 Figure 7. Mean longitudinal gradients of isoprene emission (black) and HCHO columns (color)

1092

across central Africa (3°S-3°N) at 12-15 LT in July. HCHO columns are shown for

1093

the OMI observations in 2005-2009 (orange) and from the GEOS-Chem simulations

1094

using the standard isoprene oxidation scheme (red) and the Paulot scheme (blue) in

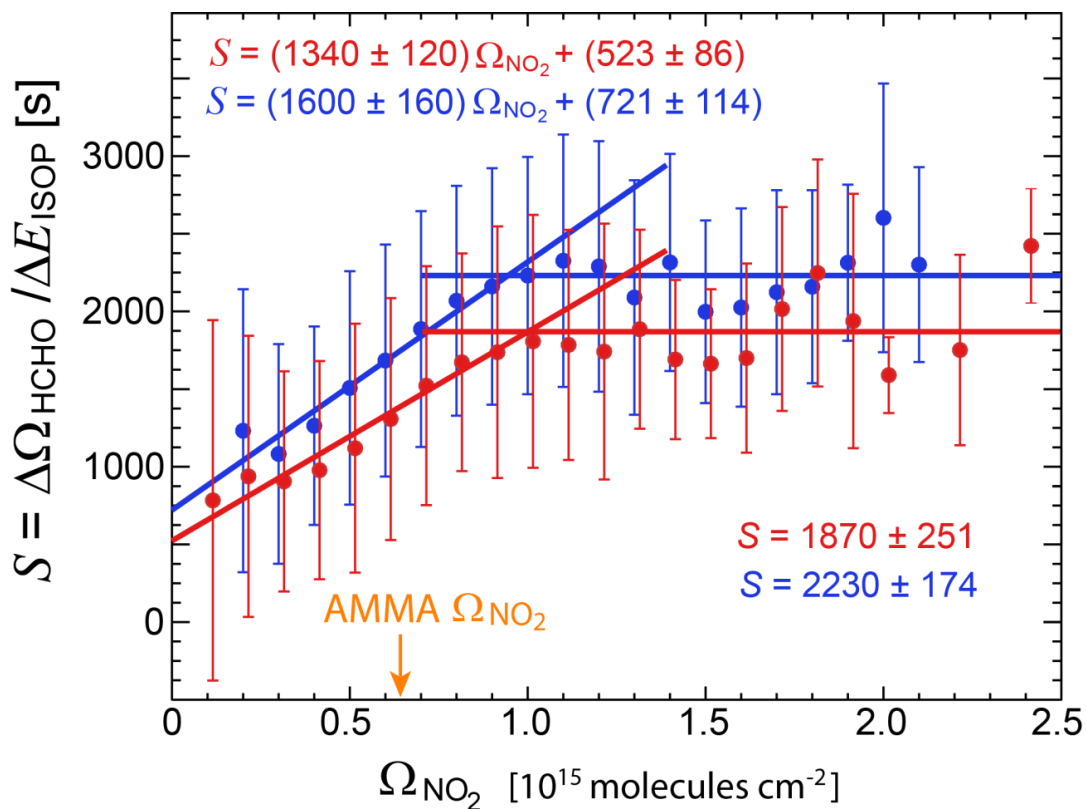
1095

2006 at 12-15 LT. Isoprene emissions are from MEGAN. The HCHO columns have

1096

been filtered against biomass burning as described in the text.

1097



1098

1099 Figure 8. Dependence of the HCHO-isoprene relationship on the local tropospheric NO<sub>2</sub>

1100 column  $\Omega_{\text{NO}_2}$  over Africa in GEOS-Chem. The figure shows statistics of  $S =$

1101  $\Delta \Omega_{\text{HCHO}} / \Delta E_{\text{ISOP}}$  computed as described in the text for individual  $2^\circ \times 2.5^\circ$  gridsquares

1102 and months in 2006 at 12-15 LT. Values of  $S$  have been sorted by the local value of

1103  $\Omega_{\text{NO}_2}$  in  $1 \times 10^{14}$  molecules  $\text{cm}^{-2}$  bins, and means and standard deviations are shown in

1104 each bin for GEOS-Chem using the standard isoprene oxidation scheme (red) and the

1105 Paulot scheme (blue). The data for  $\Omega_{\text{NO}_2} \leq 1 \times 10^{15}$  molecules  $\text{cm}^{-2}$  show a linear

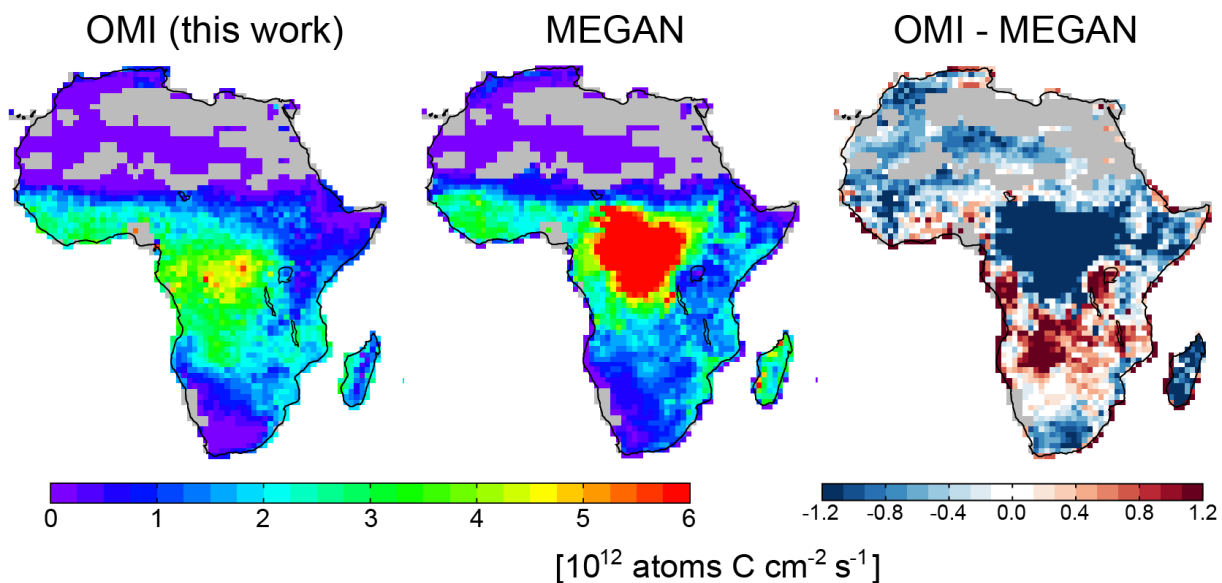
1106 relationship between  $S$  and  $\Omega_{\text{NO}_2}$ , and reduced-major-axis regression parameters are

1107 shown inset with standard deviations determined using jackknife resampling (Manly,

1108 1997). The data for  $\Omega_{\text{NO}_2} > 1 \times 10^{15}$  molecules  $\text{cm}^{-2}$  show no significant dependence

1109 between  $S$  and  $\Omega_{\text{NO}_2}$ , and the corresponding mean values and standard deviations of  $S$

1110 are shown inset. The mean and standard deviation of OMI  $\Omega_{\text{NO}_2}$  during AMMA (July-  
1111 August 2006) is also shown (orange).  
1112



1113

1114 Figure 9. Annual average isoprene emissions from Africa at  $1^\circ \times 1^\circ$  horizontal resolution at 12-  
 1115 15 LT. Values inferred from the OMI HCHO 2005-2009 data (left) are compared to  
 1116 values from the MEGAN bottom-up inventory (center). The right panel shows the  
 1117 difference between the two. Results are for the ensemble of  $1^\circ \times 1^\circ$  gridsquare-months  
 1118 that are not excluded from our analysis due to biomass burning, anthropogenic, dust,  
 1119 or smearing influences (see text). Completely excluded areas are shown in grey.